
Electronic Thesis and Dissertation Repository

1-25-2012 12:00 AM

Development of a Three-Dimensional Image-Guided Needle Positioning System for Small Animal Interventions

Christopher S.R. Waring
The University of Western Ontario

Supervisor
James Lacefield
The University of Western Ontario Joint Supervisor
Aaron Fenster
The University of Western Ontario

Graduate Program in Biomedical Engineering
A thesis submitted in partial fulfillment of the requirements for the degree in Master of Engineering Science
© Christopher S.R. Waring 2012

Follow this and additional works at: <https://ir.lib.uwo.ca/etd>



Part of the [Biomedical Engineering and Bioengineering Commons](#)

Recommended Citation

Waring, Christopher S.R., "Development of a Three-Dimensional Image-Guided Needle Positioning System for Small Animal Interventions" (2012). *Electronic Thesis and Dissertation Repository*. 375.
<https://ir.lib.uwo.ca/etd/375>

This Dissertation/Thesis is brought to you for free and open access by Scholarship@Western. It has been accepted for inclusion in Electronic Thesis and Dissertation Repository by an authorized administrator of Scholarship@Western. For more information, please contact wlsadmin@uwo.ca.

Development of a three-dimensional image-guided needle
positioning system for small animal interventions

(Spine title: Image-guided needle positioning system for small animal interventions)

(Thesis format: Integrated Article)

by

Christopher Stanley Robert Waring

Graduate Program in Biomedical Engineering

A thesis submitted in partial fulfillment
of the requirements for the degree of
Master of Engineering Science

The School of Graduate and Postdoctoral Studies
The University of Western Ontario
London, Ontario, Canada

© Christopher Stanley Robert Waring, 2012

THE UNIVERSITY OF WESTERN ONTARIO
School of Graduate and Postdoctoral Studies

CERTIFICATE OF EXAMINATION

Supervisor

Examiners

Dr. Aaron Fenster

Dr. Maria Drangova

Dr. James C. Lacefield

Dr. James Johnson

Supervisory Committee

Dr. Keith St. Lawrence

Dr. David W. Holdsworth

Dr. Shaun Salisbury

The thesis by

Christopher Stanley Robert Waring

entitled:

**Development of a three-dimensional image-guided needle
positioning system for small animal interventions**

is accepted in partial fulfillment of the
requirements for the degree of
Master of Engineering Science

Dated this 25th day of January, 2012.

Dr. Lauren Briens

Abstract

Conventional needle positioning techniques for small animal microinjections are fraught with issues of repeatability and targeting accuracy. To improve the outcomes of these interventions a small animal needle positioning system guided by micro-computed tomography (micro-CT) imaging was developed. A phantom was developed to calibrate the geometric accuracy of micro-CT scanners to a traceable standard of measurement. Use of the phantom ensures the geometric fidelity of micro-CT images for use in image-guided interventions or other demanding quantitative applications. The design of a robot is described which features a remote center of motion architecture and is compact enough to operate within a micro-CT bore. Methods to calibrate the robot and register it to a micro-CT scanner are introduced. The performance of the robot is characterized and a mean targeting accuracy of $149 \pm 41 \mu\text{m}$ estimated. The robot is finally demonstrated by completing an *in vivo* biomedical application.

Keywords

medical robotics, image-guided interventions, small animal imaging, x-ray micro-computed tomography, imaging phantom design and construction

Co-Authorship Statement

Chapter 2

Chapter 2 is in preparation to be submitted to *Medical Physics* with the author list: Christopher Waring, Jeffrey S. Bax, Amila Samarabandu, David W. Holdsworth, Aaron Fenster and James C. Lacefield. Jeff designed and constructed the calibration phantom. Jeff also developed the method to measure the calibration phantom to a traceable standard. The construction and measurement of the phantom was completed by Jeff with assistance from the laboratory machinists Jacques Montreuil and Kevin Barker. I was responsible for developing the algorithm and software for processing the micro-CT images of the phantom to characterize the scanner geometric accuracy. Amila was a summer research assistant who assisted in the development of the software. I was responsible for collecting images of the phantom and performing all image analysis. The work presented in this chapter was performed under the supervision of David W. Holdsworth, James C. Lacefield and Aaron Fenster.

Chapter 3

Chapter 3 is in preparation to be submitted to *Medical Physics* with author list: Jeffrey S. Bax, Christopher Waring, Shi Sherebrin, Shawn Stapleton, James C. Lacefield and Aaron Fenster. For this study, Jeff designed and calibrated the prototype robotic device that was constructed by our laboratory machinists: Jacques Montreuil and Kevin Barker. Shi and Jeff developed the kinematic control software for the robot. Shi was responsible for the design and construction of the electric hardware with the assistance of our electrician, Janos Bartha. Jeff and I together developed the needle calibration and robot registration methods. I was responsible for developing the methods and software to characterize the systems performance and carrying out the image analysis. I was also responsible for developing the robot registration software. Shawn acquired all of the CT images and in addition, designed and performed the animal experiments. Work on this project was performed under the supervision of James C. Lacefield and Aaron Fenster.

Dedicated to my parents

Acknowledgments

I would like to acknowledge the many people who contributed to my course of studies while at Robarts:

I would first like to thank supervisors James Lacefield and Aaron Fenster for their guidance and insight throughout my project. I would also like to thank the other members of my advisory committee: David Holdsworth and Shaun Salisbury. Special thanks to David Holdsworth for his guidance in the micro-CT calibration portion of my thesis.

Thanks also go to all of the members of the Lacefield and Fenster labs during my time at Robarts. Special thanks go to Jeff Bax who I closely collaborated with throughout the course of my research. This project would not have been possible without his knowledge and skill in mechanical design. I would also like to thank the Fenster lab machinists Jacques Montreuil and Kevin Barker who fabricated much of what is presented in this thesis. Thanks also go to Shi Sherebrin and Janos Bartha for development and construction of the robot electronic hardware. I would also like to thank Joseph Umoh, the micro-CT imaging facility manager, for patiently spending many hours helping to acquire images.

I would like to thank David Jaffray and his lab at the University Health Network for their assistance and for the use of their micro-CT scanner. I want to thank Shawn Stapleton and Mike Dunne from the Jaffrey lab for spending many long days behind the micro-CT console with Jeff and I. In addition, I would like to thank Shawn for his help in developing and performing the small animal experiments.

Finally, I would like to acknowledge my personal funding sources during the course of my degree: a scholarship from the Natural Sciences and Engineering Research Council training program in Computer Aided Medical Interventions from 2009-2011 and a Western Graduate Research Scholarship from 2009-2011.

Table of Contents

CERTIFICATE OF EXAMINATION	ii
Abstract	iii
Co-Authorship Statement.....	iv
Table of Contents	vii
List of Tables	xi
List of Figures	xii
Chapter 1	1
1 Introduction	1
1.1 Medical Robotics	1
1.1.1 Clinical Role of Medical Robotics.....	1
1.1.2 Medical Robot Architecture.....	3
1.2 Small Animal Needle Interventions.....	5
1.3 Preclinical Robotic Needle Positioning Systems.....	6
1.3.1 Current Preclinical Needle Positioning Systems	6
1.4 Preclinical Robot Workflow	8
1.4.1 Needle Calibration	8
1.4.2 Robot to Imaging Modality Registration	10
1.4.3 Needle Placement.....	13
1.5 Drawbacks of Current Preclinical Systems.....	14
1.6 X-Ray Computed Tomography.....	16
1.7 Technical Objectives.....	18
1.8 Outline of Thesis.....	19
1.8.1 Chapter 2: Traceable Micro-CT Geometric Accuracy Phantom for Applications Requiring Exact Measurement of Distances or Volumes....	19

1.8.2	Chapter 3: 3D Image-Guided Robotic Needle Positioning System for Small Animal Interventions	19
	References	21
	Chapter 2.....	29
2	Traceable Micro-CT Geometric Accuracy Phantom for Applications Requiring Exact Measurement of Distances or Volumes	29
2.1	Introduction.....	29
2.2	Methods.....	31
2.2.1	Calibration Phantom Construction.....	31
2.2.2	Measurement of Bead Positions within Calibration Phantom	32
2.2.3	Imaging the Calibration Phantom	34
2.2.4	Geometric Correction Calculation	35
2.2.5	Validation Phantom Construction.....	36
2.2.6	Data Analysis	37
2.3	Results.....	38
2.3.1	Correction Factor Values	38
2.3.2	Geometric Correction to Calibration Phantom	40
2.3.3	Geometric Correction to Validation Phantom	41
2.3.4	Comparison of Validation Phantom Errors.....	42
2.4	Discussion	42
2.5	Conclusion	45
	References	46
	Chapter 3.....	48
3	3D Image-Guided Robotic Needle Positioning System for Small Animal Interventions	48
3.1	Introduction.....	48
3.2	Methods.....	50

3.2.1	Mechatronic System Design	50
3.2.2	Robot Calibration.....	56
3.2.3	Robot to micro-CT Registration	61
3.2.4	Robot Targeting Accuracy	64
3.2.5	Preclinical Application.....	66
3.3	Results.....	67
3.3.1	Robot Calibration.....	67
3.3.2	Robot Positioning Accuracy	70
3.3.3	Preclinical Application.....	71
3.4	Discussion	74
3.4.1	Robot Calibration.....	74
3.4.2	Robot Registration	76
3.4.3	Robot Positioning Accuracy	77
3.4.4	Preclinical Application.....	80
3.5	Conclusion	80
	References	82
	Chapter 4.....	85
4	Summary and Future Work.....	85
4.1	Summary	85
4.1.1	Chapter 2: Traceable Micro-CT Geometric Accuracy Phantom for Applications Requiring Exact Measurement of Distances or Volumes....	85
4.1.2	Chapter 3: 3D Image-Guided Robotic Needle Positioning System for Small Animal Interventions	86
4.2	Conclusion	88
4.3	Future Work	89
4.3.1	Improved Software Integration and Intervention Planning	89
4.3.2	Integration of Robot with Alternative Imaging Modalities	90

4.4 Final Remarks	91
References	92
Curriculum Vitae	93

List of Tables

Table 1.1-Summary of existing image-guided small animal needle positioning systems.....	7
Table 2.1-Summary of the micro-CT scan parameters used for imaging the phantoms	34
Table 2.2-Calculated average scanner correction factors for each axis.....	38
Table 2.3-Results of Tukey test for differences in the mean correction factors for each pair of scanner axes	39
Table 2.4-Uncorrected and corrected bead separation errors for the calibration phantom.....	40
Table 2.5-Uncorrected and corrected bead separation errors for the validation phantom.....	41
Table 3.1-Summary of the results obtained for each experiment with robotic system.....	68
Table 3.2-Summary of needle angulations used to test needle deflection at different angles of attack	71

List of Figures

Figure 2.1-Micro-CT surface rendering of the a) calibration phantom and b) validation phantom.....	32
Figure 2.2- Calibration and validation phantom with measurement equipment.....	33
Figure 3.1- A schematic representation of the proposed RCM linkage design	52
Figure 3.2- (Top): Photograph of the robotic apparatus mounted on the CT scanner animal couch and control system. (Bottom): Photograph of the forward spherical linkage and attached needle driver	54
Figure 3.3- Photograph of the calibration fixture used to set the needle tip position at the RCM when the needle driver is in its forward position	60
Figure 3.4- View of reconstructed CT image used for the needle targeting experiment.....	65
Figure 3.5- Composite photographs of the calibration photos showing the pitch (Top Left) and roll (Top Right) of the needle throughout its full range of motion. The bottom two photographs shows a close-up view of the segmented needle tip locations in the pitch (Bottom Left) and roll (Bottom Right) directions.....	69
Figure 3.6- Photograph of the experimental setup used for the animal interventions (a) outside, and (b) inside of the bore of the CT scanner	72
Figure 3.7- Wick-in-needle measurements of IFP using robot positioning.....	73
Figure 3.8- Projection views obtained from two sequential CT scans which demonstrate the ability to perform image-guided needle placement <i>in vivo</i>	74
Figure 3.9- A composite image of the needle tracks from the needle angulation accuracy experiment.....	78

Chapter 1

1 Introduction

1.1 Medical Robotics

1.1.1 Clinical Role of Medical Robotics

The first demonstration of using a robot to complete a medical intervention was in 1985 at the Memorial Medical Center of Long Beach [1]. An off-the-shelf Puma 200 industrial robot was used to complete the biopsy of a suspicious brain lesion. The robotic procedure was an attempt to complete an existing procedure faster with higher reliability and accuracy. Conventionally, the biopsy procedure had been completed using a stereotactic frame based on technology first introduced in 1908 [2]. The stereotactic frame had been integrated with an x-ray computed tomography (CT) scanner. To complete the stereotactic frame procedure, the patient was first scanned using the CT scanner and the position of the lesion localized in the image. A computer then calculated four angular settings of the stereotactic frame and the depth required to position a needle tip at the lesion based upon the position of the lesion in the image. The stereotactic frame was then manually adjusted to match the calculated settings. Unfortunately, the process required to manually adjust the stereotactic frame was found to be tedious, subject to operator error and lack flexibility. To address these limitations, the Puma 200 robot was placed on the scanner bed. The robot was able to quickly and automatically position a needle bushing to correspond with the brain lesion based on a CT image. A surgeon then used the bushing to insert the needle into the lesion and successfully complete a biopsy. Although promising, this initial line of research was halted by the manufacturer of the Puma 200 on the basis that an industrial robot was unsafe for surgical applications [3].

The field of medical robotics has undergone tremendous growth since its beginnings. The number of yearly publications on the topic has experienced exponential growth since the early 1990s. In 2005 alone, new publications on medical robotics numbered over 600 [4]. This growth is demonstrated in the da Vinci robotic system (Intuitive Surgical, Sunnyvale, CA). The da Vinci is the most successful medical robot

system developed. According to its manufacturer, an installed base of over 1700 systems completed 278,000 procedures worldwide in 2010. This represented a growth of over 220% compared to the procedures completed in 2008 [5]. Furthermore, use of the da Vinci system is increasingly becoming the standard of care for completing procedures such as radical prostatectomies [6]. Along with the da Vinci, dozens of other unique robotic systems exist to complete a wide-range of medical procedures [7]. The breadth and ubiquity of medical robotics makes a concise study of the topic challenging.

A study of the nomenclature of medical robotics is one method for developing an understanding of the current-state of the field. Unfortunately, the nomenclature of medical robotics lacks convention. Authors may classify systems with a wide range of options such as mechanical design, level of autonomy or intended application [7]. Depending upon the classification system, the resulting nomenclature may become quite complicated and fractured. A useful high-level system for classifying medical robots was introduced by Camarillo *et al.* which categorizes robots based on their role in the medical procedure [8]. This nomenclature divides devices into three role categories: passive, restricted and active. The passive role consists of systems that have a limited role in the procedure or are involved in lower risk procedures. Restricted role systems are involved in higher risk procedures, but are restricted to a specific task of the procedure. Active role systems are a critical component of the procedure and are responsible for high-risk tasks. Furthermore, the authors note that each of these role categories represents an inverse trend of procedure risk to robot autonomy. Passive role systems with the lowest risk generally have the highest degree of autonomy, while active role systems with the highest risk generally have the lowest autonomy and remain under direct supervision by a surgeon. This relationship arises from the same safety concerns that in 1985 led to the end of research with the Puma 200 for brain lesion biopsy. Robotic systems that have drifted away from this trade-off between robot autonomy and procedure risk have seen little success [3,9].

Commercially available examples are provided by Camarillo *et al.* to illustrate this method of robot categorization. Throughout these examples, the trend of increasing risk with decreasing robot autonomy is evident. The CyberKnife (Accuray Inc.,

Sunnyvale, CA) is a robotic system developed to complete radiosurgery [10]. Mounted onto the CyberKnife is an x-ray linear accelerator for radiotherapy of cancer. The CyberKnife automatically sets up and registers a radiation treatment plan developed by a radiotherapist to the position of a patient using intra-operative images. The CyberKnife then autonomously positions the x-ray linear accelerator to complete the plans. During the procedure the CyberKnife never physically contacts the patient and the interaction is considered to be lower risk. As a result, the system is categorized as a passive role system. The next example in the restricted role is the RoboDoc (Curexo Technology Corporation, Fremont, CA) system [11]. The RoboDoc is used for orthopedic applications which require bone-milling, typically, total hip replacement [12]. Since RoboDoc is in direct contact with the patient, the procedure is higher risk. RoboDoc autonomously mills the bone based on a path developed by the surgeon using pre-operative CT images. However, RoboDoc is not responsible for the entire orthopedic procedure. Rather, RoboDoc is only used for a very specific portion of procedure and only carries out the single specific task of milling. Unlike the CyberKnife, the initial setup and plan registration to the patient is completed manually by the surgeon, limiting RoboDoc's autonomy. The higher risk and limited scope of the RoboDoc leads to its restricted categorization. The previously discussed da Vinci robot serves as the final example [13]. The da Vinci is a telerobot which operates using a slave-master system. A surgeon sits at the master console of the da Vinci system, which contains controls and a stereoscopic display. The surgeon uses the console to control the robotic arms of the slave system in real time during procedures. As a result, the da Vinci systems possess very little autonomy. The da Vinci is typically used to carry out entire minimally invasive procedures during which it is in constant physical contact with the patient, thus creating a high risk. The critical role of the da Vinci in completing high risk procedures places it in the active role category. These examples serve to demonstrate the range of roles medical robotics can fulfill with varying levels of autonomy and risk.

1.1.2 Medical Robot Architecture

A large range of potential architectures exist for robotic systems. Of these architectures, the remote center of motion or RCM has become one of the most

successful in medical robotics [7,14]. The RCM was first introduced to medical robotics in 1995 by Taylor *et al.* [15]. In an RCM design, the translational motion of a tool mounted onto the robot is decoupled from the rotational motion at a fixed point in space. In other words, both translational and rotational motion can be performed independently of one another. The RCM allows a tool to pivot about the fixed point in space, which is an extremely useful capability for medical applications. For example, the first RCM-based robot developed by Taylor *et al.* was developed to position tools, such as a camera, during laparoscopic surgery. In laparoscopic surgery, tools most pass through small cannulas to enter the abdomen. The translational motion of tools passing through these entry points must be constrained to avoid injury to the patient. The use of an RCM provides a perfect solution to this required constraint. The RCM can be positioned to correspond with the cannula, creating a fulcrum at the point of entry. The tool can then be freely inserted or retracted and rotated while inserted into the patient without danger of translation and injury. The RCM represents a very practical and useful robot architecture for medical applications.

An RCM point is created at the common intersection point of all the rotational axes of a robot. If all the rotational axes of a robot do not intersect, an RCM will not be formed. The RCM can be created through either active or passive means. The RCM can be created actively through programming of the robot to coordinate motion of all the joints to intersect their rotational axes at a common point [16]. However, the RCM is typically achieved passively through mechanical design and the resulting kinematics, which constrain the rotational axes to intersect at a point. A number of different mechanical designs can be used to achieve a passive RCM. A review of RCM robot designs finds the parallel-bar linkage to be the most popular mechanical design [7]. Other mechanical designs that have been used to create RCMs include the goniometric arc [17] and spherical linkage [18]. The mechanical design selected may vary depending on the application and user preference. A schematic drawing of a spherical linkage based RCM design is shown in **Chapter 3** of this thesis in **Figure 3.1**.

1.2 Small Animal Needle Interventions

Small animal models in preclinical research are critically important to expanding medical knowledge and to the development new of treatments and therapies for human disease [19]. From a regulatory standpoint, animal models are a typical requirement to demonstrate the efficacy of new treatments and therapies before clinical trials [20]. Needle interventions are a common procedure performed during the course of preclinical research. These needle interventions may be performed to inject a variety of compounds such as imaging contrast agents [21], cancer or stem cells [22,23], and other biological or therapeutic agents [24,25]. Interventions may also be required to position needle-like measurement probes within small animals for data collection [26]. Conventionally, non-robotic, manual techniques are used to complete these interventions. Typical manual interventions used to complete these interventions include: surgical exposure of the target, percutaneous injections through the skin or the use of a stereotactic device. Each of these conventional techniques possesses drawbacks that could be improved upon with the use of robotics.

Surgical exposure of targets during needle interventions allows for direct visual localization of targets. Examples of targets for surgical exposure include the pancreas [27], intestine [28], thymus [29] and heart [23]. Surgical exposure is typically reserved for interventions requiring high positioning accuracy due to the ability to visually localized targets during surgery. To improve target localization, microscopy may be used during needle positioning [28]. Unfortunately, surgical exposure has a number of drawbacks. Completion of the surgery is time consuming and requires highly trained personnel. The procedure is also subject to human error and operator variability. Surgery is highly invasive and may result in morbidity or mortality of the animal. Even if successful, surgery may still impose pain and distress on the animal causing potential immune dysfunction, behavioral changes and other negative physiological changes [30]. These changes may confound research results and make it difficult to discern the effects of the experimental procedure from the surgical side-effects.

Percutaneous injections involve the positioning of a needle through the skin without direct visual localization of the target. Percutaneous injections are simpler to

carry out and are less invasive than surgical exposure. As a result, the use of percutaneous injections is seen as a preferred alternative to surgical exposure when completing interventions. The visual target localization provided by surgery has been replaced with both anatomical landmarks [29] and ultrasound imaging [23,31] to localize targets during percutaneous injections. Although percutaneous injections reduce the side effects of procedures, they are still subject to the same issues of operator error and repeatability. For example, injections into the tail vein are perhaps one of the most common percutaneous injection procedures completed. However, no standard methods exist to quantify operator competence or the success of a tail vein injection. Therefore, the success and effectiveness of the common tail vein injection is poorly monitored and the failure rate potentially underestimated [32].

Stereotactic frames are typically used for positioning needles or probes within the skull. The design of most modern stereotactic frames is based off the Horsley-Clarke apparatus developed in 1908 [2]. Anatomical atlases, such as the Paxinos atlas for mice [33], are typically used for needle guidance during stereotactic procedures. The atlases provide information to determine an appropriate needle insertion point in the skull and to localize a specific anatomical landmark within the brain. The Cartesian coordinate system of the stereotactic frame is then manually adjusted to locate the needle at the position specified by the atlas. The manual adjustment of the frame is vulnerable to operator error and positioning errors. As previously discussed, the potential for errors in manual adjustment of stereotactic frames was a driving factor in the development of the first clinical robotic intervention in 1985 [1]. Furthermore, deviations of the true animal anatomy from an atlas can occur with different strains of animals [34] or animals of varying sizes [35]. These deviations can result in the erroneous localization of targets for interventions.

1.3 Preclinical Robotic Needle Positioning Systems

1.3.1 Current Preclinical Needle Positioning Systems

A number of image-guided robotic needle positioning systems have been developed to complete small animal needle intervention techniques. The robotic systems

Table 1.1-Summary of existing image-guided small animal needle positioning systems.

Initial Author	Year	Mechanical Design	DOF	RCM?	Imaging Modality	Mean Free-Space Positioning Accuracy (μm)	Mean Image-Guided Positioning Accuracy (μm)	Ref.
Huang <i>et al.</i>	2006	Commercial desktop robot	4 Translational 1 Rotational	No	MR/PET	50 ± 12	1200 ± 390	[37]
Waspe <i>et al.</i>	2007	Custom parallel four-bar linkage	4 Translational 2 Rotational	Yes	CT/US	54 ± 12 (Pitch axis plane) 91 ± 21 (Roll axis plane)	157 ± 113 (CT) 550 ± 112 (US)	[38],[39], [40]
Kazanzides <i>et al.</i>	2007	Custom design using commercial linear stages	4 Translational	No	PET	48 ± 7 (3 Translational Axes) 75 ± 30 (1 Translational Axis)	< 400 (overall) 200 (near registration fiducials)	[41],[42]
Nicolau <i>et al.</i>	2007	Industrial articulated arm robot	6 Rotational	No	CT	N/A	N/A	[43],[44]
Ramrath <i>et al.</i>	2008	Custom stereotactic frame/ goniometric arc	3 Translational 2 Rotational	Yes	N/A	32 ± 11	N/A	[45],[46]
Bebek <i>et al.</i>	2008	Custom parallel gimbal joints	5 Rotational	No	N/A	419 ± 166	N/A	[47], [48]

seek to complete needle interventions with greater reliability, accuracy and repeatability over the conventional techniques. To achieve these goals, the positioning systems take advantage of the wide range of commercially available small-animal imaging systems [21]. The robots are coupled with these specialized imaging systems to accurately and non-invasively localize targets. Although similar clinical robotic systems exist, small-animal preclinical systems are unique amongst medical robots. Typical clinical image-guide needle positioning systems are required to achieve targeting accuracies on the scale of 1-2 mm [36]. Preclinical needle positioning systems may be required to achieve an order of magnitude finer targeting accuracies of $< 200 \mu\text{m}$ to reach some targets [38]. The preclinical systems also defy the traditional trade-off between autonomy and risk found in clinical robotic systems. The developed preclinical systems perform high risk procedures with a high level of autonomy. The robots are fully responsible for positioning needles into target positions localized by the user. The high targeting accuracy requirements and unique role of the preclinical robots prevents direct translation of existing medical robotic systems for the application. Rather, unique robotic needle positioning systems must be developed.

Table 1.1 summarizes the current literature of preclinical robotic needle positioning systems. The table serves to highlight that the field is in its infancy. Robotic systems for small-animal applications have only emerged in the past decade and appeared

nearly 20 years after the first clinical robotic systems. Many of the robots remain works-in-progress and their performance has yet to be characterized when coupled with small-animal imaging systems. The number of preclinical robots developed is also small compared to the dozens of available clinical systems [7]. Similar to early clinical robotics, many of the preclinical systems implement off-the-shelf commercial or industrial robots. The use of the RCM architecture has carried over from clinical robots in several of the custom-designed preclinical robots. Generally, the workflow for completing interventions using these preclinical robotic systems can be divided into three discrete steps: needle calibration, robot registration to the imaging modality and finally needle placement. The process for completing each of these steps and the metrics used to evaluate their success are discussed in the following sections.

1.4 Preclinical Robot Workflow

1.4.1 Needle Calibration

Needle calibration is the process of ensuring the true position of the needle tip matches as closely as possible its expected position based on robot kinematics. Needle calibration must be performed on a semi-regular basis whenever a new needle or tool is placed on the robot. Currently, no standardized method or metric exists to complete and characterize needle-tip calibration. Rather, each robotic system has its own unique calibration process and method for characterizing the results. However, optical based methods have been the preferred choice for completing the calibrations. The calibration methods can also be sub-divided between robots with an RCM design and robots with a non-RCM design. Differences between the RCM and non-RCM architectures dictate slightly different calibration methods. The focus of this discussion will be on calibration of RCM designs.

The purpose of the RCM architecture is to constrain the motion of a needle-like tool to a single fulcrum point in space. To achieve this goal, the tool tip of an RCM-based robot design must as closely as possible correspond with the RCM point in space. If the tool does not correspond with the RCM, undesirable translation of the tool will occur. Therefore, the process of calibration in RCM designs is the process of matching

the tool with the robot RCM. When perfectly calibrated, a desired point on the tool should remain stationary in space as the robot's rotational axes are adjusted. The two identified RCM robot designs of Waspe *et al.* [38] and Ramrath *et al.* [45] take somewhat similar approaches to needle calibration. The methods recognize that an RCM design constrains the motion of a tool tip to a near sphere when it is at an assumed RCM point with a centre of rotation at the true RCM. The larger the radius of the sphere, the further the tool is from the RCM point and the larger the calibration error. Central to both calibration methods is measurement of the needle centre of rotation. The centre can be measured by calculating the travel of the needle throughout the robot's full rotational range of motion. In both calibration methods, the positions of the needle are determined using cameras.

The method of Ramrath *et al.* uses two cameras positioned 90 degrees apart. The cameras concurrently collect images of a microelectrode tip mounted onto the robot. The two rotational axes of the robot are independently adjusted at predefined angles. The resulting motion of the needle for each of the angular adjustments is measured by segmenting the needle tip using an unspecified edge detection algorithm. Using the measured needle motions, appropriate offset corrections can be calculated using least squares to position the needle back to the RCM. Thus, when the tool tip is rotated the offset corrections are simultaneously applied to match the tip to the RCM. Unfortunately, no metric is provided to evaluate the effectiveness of the calibration. Only the total positioning accuracy of robot of $32 \pm 11 \mu\text{m}$ in free space is provided, which incorporates multiple error sources including the calibration error [45].

The method developed by Waspe *et al.* uses a camera to photograph a needle in two planes 90 degrees apart and perpendicular to each of the robot's rotational axes. In each plane, the needle is again photographed at a set of predetermined angles along each of the rotational axes. The needle is then segmented in each of the photographs using a Sobel edge detector. Unlike Ramrath *et al.*, the needle centerline was calculated in the photographs rather than the tip. In each plane, the centerlines are assumed to be tangential to a circle with the RCM at the centre. The radius of the circle represents the calibration error. An iterative process of adjusting and re-photographing the needle is

used until the radius of the circle in both planes is minimized. Unsurprisingly, the iterative process is time consuming and may require one hour to calibrate the robot. The calibration was evaluated by reporting the radius of circles in each plane: $\Delta x = 35 \pm 14 \mu\text{m}$, $\Delta y = 8 \pm 21 \mu\text{m}$ and $\Delta z = 8 \pm 11 \mu\text{m}$ [38]. Where Δx is the horizontal distance for the pitch axis, Δy is the horizontal distance for the roll axis and Δz is the vertical distance for both axes. Figures illustrating these axes can be found in figures 2 and 5 of Waspe *et al.* [38].

Non-RCM robot designs cannot make the same assumptions regarding inherent constraints on the motion of the needle as in RCM designs. As a result, the calibration methods used are slightly different from RCM designs. However, similar to RCM designs, the use of optical methods remains a popular option for calibration. The robotic systems by Bebek *et al.* [48] and Nicolau *et al.* [44,49] both implement optical solutions for calibration.

1.4.2 Robot to Imaging Modality Registration

Registration is the step that integrates the robotic system with an imaging system for guidance. Development of a registration process is a particularly challenging step in robot development. This is demonstrated by **Table 1.1**, which shows only half of the existing robot systems have been demonstrated using image-guidance. The registration process determines how to best transform a coordinate in the image to match the same point in space in robot coordinates. Once the transform is calculated, it can then be used to direct the robotically manipulated tool to a target localized within the image. The registration between the two coordinate systems is calculated using sets of fiducials. Within the current context, a fiducial is a point of reference whose position can be determined in both image and robot coordinates. A set of two corresponding coordinates for a group of fiducials enables the transformation between the image and robot coordinate systems to be calculated. The registration process uses several standardized metrics for evaluating the quality of the registration. Although current work on preclinical robot to image registration has been limited, several different approaches have been taken to complete the registration process for several imaging modalities. Two

methods of particular interest are by Kazanzides *et al.* and Waspe *et al.* to register a robotic system to CT imaging systems.

The first step in the registration process is localizing the two sets of coordinates for fiducials. The two techniques take very different approaches for localizing fiducials. Kazanzides *et al.* [41] developed a registration process which claims to be compatible with all imaging systems including PET, SPECT, CT and MRI. However, the process has only been demonstrated using PET imaging. The registration process uses a bed onto which animals are secured. The animal bed contains four small hemispherical fiducial markers. The markers contain an appropriate contrast agent for the imaging modality. The animal bed is imaged with the fiducials and the position of the high contrast fiducials in the image measured using an unspecified image processing algorithm. The animal bed is next placed in the robot workspace. The user then manually determines the position of the markers in robot coordinates by moving the robot until a probe contacts the marker. Waspe *et al.* [39] developed a registration technique specific for CT. The CT registration is performed by instructing the robot to position a needle at several specified positions in a gel phantom. The needle is then slowly retracted from the gel at each position while it injects barium, an x-ray contrast agent, into the needle track. The coordinates of the barium in robot coordinates are assumed to match the needle path. The barium tracks are then imaged using the CT scanner. Within the image, each track was segmented slice-by-slice using a 2-D threshold based region growing. Points along each needle track in the image were calculated by determining the centroid of the tracks in each image slice.

The second step of the registration process is determining the transformation between the two sets of fiducials coordinates. Kazanzides *et al.* and Waspe *et al.* both used a point-based rigid-body registration to determine the transformation. “Point-based” implies that the registrations are calculated using points rather than other shapes or surfaces. “Rigid-body” registration assumes that the transformation between the two coordinate systems consists of only translation and rotation. The rigid-body registration consists of six degrees of freedom: 3 translational and 3 rotational. Although a large number of different registration methods exist, the rigid body registration appears to be the most popular in the few existing preclinical robotic systems. Kazanzides *et al.*

calculated the rigid body registration using a least-square fit [50]. The fit was calculated by determining the transformation that minimized the difference between the known fiducial robot coordinates and the fiducial image coordinates after transformation into robot coordinates. Waspe *et al.* required the slightly different method of using the iterative close point (ICP) algorithm for calculating the rigid body registration [51]. A different method was required since a direct one-to-one correspondence between the two sets of coordinates no longer existed. Rather, a set of segmented image points was registered to the line of the needle track in robot coordinates. The ICP algorithm iteratively uses a least-squares fit between the set of image points to the nearest neighboring point on the robot track line. The iterative algorithm is repeated until the change in error from registration to registration is minimized. The user must also manually initialize the ICP algorithm with an initial rigid-body registration.

The final step in registration is evaluating the quality of the registration. The three metrics generally used to characterize a registration are: fiducial localization error (FLE), fiducial registration error (FRE) and target registration error (TRE) [52]. FLE represents the error in measuring the coordinates of the fiducials, i.e., how accurately the two sets of fiducial coordinates were measured. FRE is the root-mean-square distance between the transformed coordinate of a fiducial and its known corresponding coordinate in that new coordinate system, i.e., how well the transformation predicts the position of fiducials. The transformation of a registration is calculated by definition to minimize FRE. The FRE is dependent on the number of fiducials used in the registration and the FLE. However, FRE is not dependent on the fiducial configuration. FRE is considered to be a somewhat unreliable metric that may report a small error for a poor registration [53]. As a result, TRE is considered to be a more reliable metric for evaluating registrations and more representative of the quality of the registration. TRE is similar to FRE, however, it is the root-mean-square distance for points which were not used as fiducials in calculating the transformation. In addition to being dependent on the fiducial number and FLE, TRE is also dependent on the fiducial configuration [53]. TRE can be reduced by increasing the fiducial number and by spreading fiducials apart with the centroid of the configuration near the desired target point [54]. For CT registration, Waspe *et al.* reported an FRE and TRE of 96 μm and 210 μm , respectively. For PET

registration, Kazanzides *et al.* reported an FRE and TRE of 240 μm and $290 \pm 100 \mu\text{m}$, respectively.

1.4.3 Needle Placement

The final step in the small-animal image-guided robot workflow is positioning of the needle to the target. The animal is first imaged by a small-animal imaging system. Generally, the robots are too large to operate within the bore of these imaging systems. As a result, the animals must be affixed to custom beds that can fit in the imaging system and then be transported to the robot workspace following imaging [39,41]. The location of the target is identified in the image and the transformation from the registration used to determine the corresponding target position in robot coordinates. The robot is then used to position the needle to the target.

Currently, only three of the existing preclinical robotic systems have been demonstrated using image-guidance to position a needle to a target. The targeting accuracy in the three systems was evaluated by measuring the mean error between the location of the needle and the desired target. Huang *et al.* used MR image guidance to position a needle to targets in a gel phantom. The authors reported a targeting accuracy of $1200 \pm 390 \mu\text{m}$ [37]. However, the method used to quantify the accuracy was not described. Kazanzides *et al.* used PET guidance to position a probe in air at holes drilled into a Delrin plastic phantom. The robot positioned the probe to the center of the holes using their expected position from the registration. The robot was then manually adjusted as needed, using visual magnification, until the probe actually corresponded with the center of the hole. The targeting error was then defined as the distance required to manually adjust the probe to the hole center. Using this method, a targeting accuracy of under 400 μm was measured [41]. The final measurement of robot positioning accuracy was described by Waspe *et al.* for both CT and ultrasound. For both cases, a tissue-mimicking phantom was created with an intersecting grid of air tubes. The intersection points of the air tubes were selected as targets and their position localized using either CT or ultrasound. Using a registration to determine the appropriate robot coordinate, the robot then inserted a needle to the phantom at each target. The needle was then retracted while injecting barium, an x-ray contrast agent, to fill the needle track. Following the

experiment, both the CT-guided and ultrasound-guided phantoms were imaged using CT. The targeting accuracy was then measured as the distance of the barium-filled needle track to the air-tube intersection target. This method yielded targeting accuracies for CT and ultrasound guidance of $157 \pm 113 \mu\text{m}$ and $550 \pm 112 \mu\text{m}$ respectively [39,40].

1.5 Drawbacks of Current Preclinical Systems

To achieve popular use, image-guided small animal needle positioning systems must achieve two objectives. First, the systems must possess an ideal targeting error of $< 200 \mu\text{m}$ [38] with high repeatability. Second, the systems must make the completion of an intervention as quick and user-friendly as possible. Without a high level of accuracy and repeatability, the robotic systems are no better than the conventional manually techniques they are meant to replace. Poor usability and user-friendliness would render the systems unwieldy, cumbersome and avoided by their potential users. As previously discussed, the development of specialized small animal preclinical robots is in its infancy. As a result, a number of potential refinements exist to improve the robotic systems in achieving these goals.

The existing robot calibration methods, particularly for RCM designs, have achieved impressive calibration results. Ramrath *et al.* developed a method which allowed their system to achieve a positioning error of $32 \pm 11 \mu\text{m}$ in free space. Waspe *et al.* was able to achieve a total calibration error of under $50 \mu\text{m}$. These calibration methods are very capable of allowing a robotic system to achieve a $200 \mu\text{m}$ targeting error. However, the methods lack user-friendliness. The method by Waspe *et al.* requires an iterative calibration that requires approximately one hour to complete. Ramrath *et al.* do not specify a length of time to complete calibration. However, this method also requires multiple iterations of adjusting a needle angle and measuring the resulting movement. Finally, both methods require possession of additional photography equipment and specialized software to complete the calibration. Although existing calibration methods achieve impressive results, room for improvement exists in reducing the amount of time and additional equipment required to complete the calibration.

The current methods to integrate and register robots with small-animal imaging systems have tended to include inherent sources of variability such as opportunities for operator error or the detachment and reattachment of animal beds. This variability ultimately impacts the robot targeting accuracy and repeatability. None of robots which have been demonstrated using image guidance have been compact enough to operate within the bore of a preclinical imaging system [37,39,41]. As a result, these systems have required the use of custom animal beds which are first attached to the scanner, then detached after imaging and finally attached to the robot. The animal bed attachment process introduces variability to both the registration and targeting process [39]. The transportation process can cause the shifting of fiducials and targets between imaging and robot interventions. The individual registration processes also possess their own unique sources of variability. Kazantzides *et al.* require that the user manually guide the robot to fiducials during registration, introducing operator error and variability which the robotic systems are attempting to reduce. Waspe *et al.* uses needle tracks filled with barium in a tissue-mimicking to perform the registration. This process introduces a number of sources of variability such as needle deflection and inconsistencies in barium flow within the needle track. These sources of variability will result in variations in registration quality. Variation in quality between registrations will lead to issues of repeatability and consistency in comparing the targeting results between the same interventions completed with different registrations.

Achieving a targeting accuracy of less than 200 μm using image guidance remains a challenge within the small-animal robots. The system developed by Waspe *et al.* is the only one to have demonstrated this desired level of performance. Using CT image-guidance, a targeting accuracy of $157 \pm 113 \mu\text{m}$ was achieved. Unfortunately, although the mean error was under 200 μm , this system still suffers from issues of repeatability as demonstrated by the large standard deviation of 113 μm . This variation can be attributed to a wide range of sources inherent to the robot including calibration error, registration error, needle deflection and mechanical design. A lack of rigidity in mechanical design can result in deflection of the robot frame and variability in targeting accuracy. The variation can also be attributed to the method of evaluating the targeting accuracy. The accuracy was determined by measuring the distance of barium filled

needle tracks to targets in a tissue-mimicking phantom. Variability in barium flow and how it filled the needle track would have also introduced variability into the targeting error. Achieving a targeting accuracy of $< 200 \mu\text{m}$ without significant variations in the accuracy remains a significant challenge to small-animal image guided needle positioning systems.

1.6 X-Ray Computed Tomography

Within this thesis, particular interest is placed on the use of CT imaging for guidance in small animal interventions. The forerunner of CT imaging was planar x-ray imaging. Planar x-ray imaging is the earliest medical imaging modality. The first clinical uses of planar x-ray images were within days of Wilhelm Conrad Röntgen publicly announcing his discovery of x-rays in 1895 [55]. Planar x-ray images are created by irradiating a specimen of interest. The intensity of the x-rays beams are attenuated as they pass through the specimen. The attenuation is the result of the specimen absorbing and scattering the x-rays. The amount of attenuation is predicted by the attenuation coefficient of the respective tissues within the specimen. The value of the attenuation coefficient increases with tissue density and atomic number and decreases with the x-ray energy. A detector can then be placed opposite the x-ray source on the other side of the tissue. The detector measures the intensity of the attenuated x-ray beams to create an image which displays the measured beam intensities [56]. The best visualized tissues with the greatest contrast in x-ray images are highly attenuating tissues such as bone and poorly attenuating tissue such as air-filled lung.

In 1972, x-ray imaging underwent a revolutionary change with the introduction of the first CT imaging systems [57]. The significance of the advancement led to the inventors of CT being awarded the Nobel prize in 1979. In planar x-ray imaging, the position of the x-ray source and detector remain fixed and acquire a single x-ray projection of the specimen. In CT-imaging, the x-ray source and detector are mounted onto a rotating gantry. The rotating gantry allows the acquisition of x-ray projections 360° around the specimen. A computer is then used to reconstruct the acquired data into tomographic images of the specimen, typically using a filtered back-projection algorithm [58,59]. A 3-dimensional CT image represents the attenuation of the x-rays for

individual sample volumes, called voxels, within the specimen. This is in comparison to planar x-ray images, which represent the total attenuation of the x-rays along a line passing through the complete specimen. Within CT images, the attenuation values are typically scaled to the Hounsfield scale (HU) [57]. In the Hounsfield scale, water is scaled to 0 HU and air to -1000 HU. Soft tissues typically range from -100 HU to 100 HU and bone is typically approximately 1000 HU.

The initial impact of CT technology was limited in the field of small animal imaging. Images acquired by typical clinical CT systems yield isotropic voxel sizes on the magnitude of 1 mm. However, the size of small-animals when compared to humans in clinical applications requires a scaling down of voxel sizes to achieve equivalence of images. Small-animal imaging applications required an order of magnitude finer isotropic voxel size of 100 μm or less [60]. This issue was solved with the introduction of the first micro-CT system with μm scale voxel sizes in 1982 [61]. Micro-CT has since developed into a popular research tool experiencing exponential growth in yearly publications and commercial availability from at least a dozen manufacturers [62]. Typical scanners are available with voxel sizes ranging from 5 μm to 450 μm and trans-axial fields of view ranging from 1 to 20 cm [63].

A critical consideration for using micro-CT in image-guided small animal interventions is the geometric accuracy of the images. Geometric inaccuracy in the images will result in incorrect target localization and a poor targeting accuracy. Previously, micro-CT scanners have been reported as possessing in-plane geometric inaccuracies of 0.2% [64] and 0.3% [65]. Over a 2 cm robot range of motion, these reported inaccuracies correspond with a 40 μm to 60 μm error. Such an error would reduce the ability of a small-animal robotic system in achieving the desired overall targeting error of < 200 μm . The ability to quickly validate the geometric accuracy of micro-CT scanners is an important tool for end users to ensure the best performance of small animal image-guided robotic systems. Two quality assurance phantoms by Du *et al.* [64] and Perelli *et al.* [66] have been previously developed to characterize the geometric errors of micro-CT scanners. Unfortunately, these phantoms have a number of drawbacks including: not being verified to a traceable standard, no method to correct

detected errors in the image and are too large to be easily integrated into the design of a robot. Therefore, at present, the ability of robot system users to validate the micro-CT geometric accuracy is limited.

1.7 Technical Objectives

The objective of this research is the development of a micro-CT guided small-animal robotic needle positioning system to improve the outcomes and efficiency of small animal needle interventions. The system must be able to achieve a mean targeting accuracy of under 200 μm with high repeatability to ensure successfully interventions. Equally important, the system must be user-friendly. Use of the system must be as quick and easy as possible to encourage its adoption by preclinical researchers and to maximize potential efficiency gains from use of the system. The specific objectives of this thesis are:

1. Develop a method which can quickly characterize the geometric accuracy of micro-CT scanners to a traceable standard and provide geometric corrections as needed.
2. Demonstrate a micro-CT guided robotic system capable of completing needle interventions. This includes: developing a method to calibrate the system, integrating and registering the robot with an imaging system, characterizing the targeting accuracy of the system and demonstrating the use of the system to complete an *in vivo* biomedical application.

1.8 Outline of Thesis

1.8.1 Chapter 2: Traceable Micro-CT Geometric Accuracy Phantom for Applications Requiring Exact Measurement of Distances or Volumes

This chapter describes the design and construction of a calibration phantom for the routine evaluation of the geometric accuracy of micro-CT scanners. The phantom consists of six fiducials whose positions have been measured to a known and traceable standard of measurement. Software is described to evaluate the geometric accuracy of micro-CT scanners by comparing the known positions of the fiducials to their positions in micro-CT images. The software calculates correction factors for each of the scanner's three axes using a least squares solution to minimize the geometric error of the fiducial positions. The correction factors are then applied to images of a second validation phantom to evaluate their ability in reducing the geometric error of images independently of the calibration phantom. The calibration phantom is used to characterize the geometric accuracy of five different micro-CT scanners representing four different micro-CT models. Statistical analysis is performed to evaluate the performance of the calibration phantom and to describe the nature of the geometric errors encountered.

1.8.2 Chapter 3: 3D Image-Guided Robotic Needle Positioning System for Small Animal Interventions

This chapter describes the design, construction, characterization and biomedical application of a micro-CT guided small animal needle positioning system. The mechanical design of the system is based upon a spherical linkage previously used in clinical applications [18]. The spherical linkage design is compact enough to allow the robot to perform interventions entirely within the micro-CT bore. A method to calibrate the robot needle is introduced which greatly reduces the time requirements of calibration compared to previous designs. A dual mode registration process is introduced to integrate the robot with a micro-CT scanner. The dual registration modes allow the user to balance registration accuracy with the time required to perform the registration

depending on the specific application. The targeting accuracy of the robot is then characterized using tissue-mimicking phantoms. Finally, use of the robot for a selected biomedical application is demonstrated.

References

- [1] Y.S. Kowh, J. Hou, E.A. Jonckheere and S. Hayati, "A robot with improved absolute positioning accuracy for CT guided stereotactic brain surgery," *IEEE Trans. Biomed. Eng.*, 35(2), 153-160 1988.
- [2] V. Horsley and R. H. Clarke, "The structure and function of the cerebellum examined by a new method," *Brain*, 31(1), 45–124, 1908.
- [3] B. Davies, "A review of robotics in surgery," *Proc. Inst. Mech. Eng. H J. Eng. Med.*, 214(1), 129-140 (2000).
- [4] N.G. Hockstein, C.G. Gourin, R.A. Faust, D.J. Terris "A History of robots: from science fiction to surgical robotics," *J. Robotic Surg.*, 1(2), 113-118, 2007.
- [5] Intuitive Surgical Inc., *2010 Annual Report*, February, 2011.
- [6] K.B. Stitzenberg, Y. Wong, M. E. Nielsen, B.L. Egleston and R.G. Uzzo, "Trends in Radical Prostatectomy: Centralization, Robotics, and Access to Urologic Cancer Care," *Cancer*, In Press, 2011.
- [7] R. H. Taylor and D. Stoianovici, "Medical Robotics in Computer-Integrated Surgery," *IEEE Trans. Robot. Autom.*, 19(5), 765–781, 2003.
- [8] D.B. Camarillo, T.M. Krummel and J.K. Salisbury, "Robotic technology in surgery: past, present and future," *Am. J. Surg.*, 188 (Suppl to October 2004), 2s-15s, 2004.
- [9] P. Dario, B. Hannaford and A. Menciassi, "Smart Surgical Tools and Augmenting Devices," *IEEE Trans. Robot. Autom.*, 19 (5), 782- 792, 2003.
- [10] J.R. Adler Jr, M.J. Murphy, S.D. Chang and S.L. Hancock, " Image-guided robotic radiosurgery," *Neurosurgery*, 44(6) ,1299–1307, 1999.

- [11] R.H. Taylor, B.D. Mittlstadt, P.W. Hanson, P. Kazanzides, J.F. Zuhars, W. Williamson, B.L. Musits, E. Glassman and W.L. Bargar, "An Image-Directed Robotic System for Precise Orthopaedic Surgery," *IEEE Trans. Robot. Autom.*, 10(3), 261-275, 1994.
- [12] A.P. Schulz, K. Seide, C. Queitsch, A. Von Haugwitz, J. Meiners, B. Kienast, M. Tarabolsi, M. Kammal and C. Jürgens, "Results of total hip replacement using the Robodoc surgical assistant system: clinical outcome and evaluation of complications for 97 procedures," *Int. J. Robotics Comput. Assist. Surg.*, 3(4), 301-306, 2007.
- [13] G. S. Guthart and J. K. Salisbury, "The intuitive telesurgery system: Overview and application," *Proc. IEEE Int. Conf. Robotics and Automation*, 2000, pp. 618-621.
- [14] C.H. Kuo and J.S. Dai in *International Symposium on History of Machines and Mechanisms*, edited by H.S. Yan and M.Ceccarelli (Springer, Netherlands, 2009), pp. 337-354.
- [15] R.H. Taylor, J. Funda, B. Eldridge, K. Gruben, D. LaRose, S. Gomory, M. Talamini, L.A. Kavoussi and J.H. Anderson, "A telerobotic assistant for laparoscopic surgery," *IEEE EMBS Mag.*, 14(3), 279-291, 1995.
- [16] L. Yang, C.B. Chng, C.K. Chui and D.P.C. Lau, "Remote center of motion in minimally invasive surgery," *Proc. IEEE Int. Conf. Robotics and Automation*, 2010, pp. 84-89.
- [17] K. Masamune, E. Kobayashi, Y. Masutani, M. S Suzuki, T. Dohi. H. Iseki and K. Takaura, "Development of an MRI-compatible needle insertion manipulator for stereotactic neurosurgery," *J. Img. Guided Surg.*, 1(4), 242-248, 1995.
- [18] J. Bax, D. Cool, L. Gardi, K. Knight, D. Smith, J. Montreuil, S. Sherebrin, C. Romagnoli and A. Fenster. "Mechanically assisted 3D ultrasound guided prostate biopsy system," *Med. Phys.*, 35(12), 5397-5410, 2008.

- [19] J.F. Pritchard, M. Jurima-Romet, M.L.J. Reimer, E. Mortimer, B. Rolfe and M.N. Cayen, "Making better drugs: decision gates in non-clinical drug development," *Nat. Rev. Drug Discov.*, 2, 542-553, 2003.
- [20] ICH: International Conference On Harmonization Of Technical Requirements For Registration Of Pharmaceuticals For Human Use, "*Guidance On Nonclinical Safety Studies For The Conduct OF Human Clinical Trials And Marketing Authorization For Pharmaceuticals*", Step 2 Version, 2008.
- [21] G.C. Kagadis, G. Loudos, K. Katsanos K, S.G. Langer and G.C. Nikiforidis, "In vivo small animal imaging: current status and future prospects," *Med. Phys.*, 37(12), 6421-6437, 2010.
- [22] G. Francia, W. Cruz-Munoz, S. Man, P. Xu and R.S. Kerbel, "Mouse models of advanced spontaneous metastasis for experimental therapeutics," *Nat. Rev. Cancer.*, 11, 135-141, 2011.
- [23] M.L. Springer, R.E. Sievers, M.N. Viswanathan, M.S. Yee, E. Foster, W. Grossman, and Y. Yeghiazarians. "Closed-chest cell injections into mouse myocardium guided by high-resolution echocardiography," *Am. J. Physiol. Heart Circ. Physiol.*, 289(3), H1307-14, 2005.
- [24] C.R. Chu, C.H. Coyle, C.T. Chu, M. Szczodry, V. Seshadri, J.C. Karpie, M.M. Cieslak and E.K. Pringle, "In vivo effects of single intra-articular injection of 0.5% bupivacaine on articular cartilage", *J. Bone Jt. Surg.*, 92(3), 599-608, 2010.
- [25] F.E. Cone, S.E. Gelman, J.L. Son, N.E. Pease and H.A. Quigley, "Differential susceptibility to experimental glaucoma among 3 mouse strains using bead viscoelastic injection," *Exp. Eye. Res.*, 91(3), 415-424, 2010.
- [26] M. Urano, Y. Chen, J. Humm, J. A. Koutcher, P. Zanzonico, C. Ling, "Measurements of tumor tissue oxygen tension using a time-resolved luminescence-based optical OxyLite probe: comparison with a paired survival assay," *Radiat. Res.*, 158(2), 167-173, 2002.

- [27] M. El-Ghamari, F. Bergmann, B.M. Schmied, J. Weitz, and A. Ulrich, "Islet cells contribute to pancreatic carcinogenesis in an animal model," *Pancreas*, 40(2), 242-246, 2011.
- [28] M.V. Cespedes, C. Espina, M.A. Garcia-Cabezas, A. Trias, A. Boluda, M.T. Gomez del Pulgar, F.J. Sancho, M. Nistal, J.C. Lacal, and R. Manges, "Orthotopic microinjection of human colon cancer cells in nude mice induces tumor foci in all clinically relevant metastatic sites," *Am. J. Pathol.*, 170(3), 1077-85, 2007.
- [29] T. de la Cueva, A. Naranjo, E. de la Cueva, and D. Rubio, "Refinement of intrathymic injection in mice," *Lab Anim.*, 36(5), 27-32, 2007.
- [30] Committee On Recognition and Alleviation of Pain in Laboratory Animals, National Research Council. *Recognition and Alleviation of Pain in Laboratory Animals*, National Academies Press, Washington D.C., 2009.
- [31] R. Blair-Handon, K. Mueller, and S. Hoogstraten-Miller, "An alternative method for intrathymic injections in mice," *Lab Animal*, 39(8), 246-252, 2011.
- [32] E.V. Groman and C.P. Reinhardt, "Method to quantify tail vein injection technique in small animals," *J. Am. Assoc. Lab Anim. Sci.*, 43(1), 35-38, 2004.
- [33] G. Paxinos and K.B.J. Franklin, *The Mouse Brain in Stereotaxic Coordinates*, Elsevier Academic Press, New York, 2008.
- [34] D. Wahlsten, W. J. Hudspeth, and K. Bernhardt, "Implications of genetic variation in mouse brain structure for electrode placement by stereotaxic surgery," *J. Comp. Neurol.*, 162(4) , 519-31, 1975.
- [35] G. Paxinos, C. Watson, M. Pennisi and A. Topple, "Bregma, lamda and the interaural midpoint in stereotactic surgery with rats of different sex, strain and weight", *J. Neuro. Sci. Meth.*, 13(2), 139-143, 1985.

- [36] K. Cleary, A. Melzer, V. Watson, G. Kronreif and D. Stoianovici, "Interventional Robotic Systems: Applications and technology state-of-art," *Minimally Invasiv. Ther.* 14 (2), 101–113, 2006.
- [37] Y. Huang, T.H. Wu, M.H. Lin, C.C. Yang, W.Y. Guo, Z.J. Wang, C.L. Chen and J.S. Lee, "An automated robot arm system for small animal tissue biopsy under dual-image modality," *Nucl. Instr. Meth. Phys. Res. A*, 569(2), 230-234, 2006.
- [38] A.C. Waspe, H. J. Cakiroglu, J.C. Lacefield and A. Fenster A, "Design, calibration and evaluation of a robotic needle-positioning system for small animal imaging applications," *Phys. Med. Biol.*, 52(7), 1863–1878, 2007.
- [39] A.C. Waspe, D.D. McErlain, V. Pitelka, D.W. Holdsworth, J.C. Lacefield and A. Fenster, "Integration and evaluation of a needle-positioning robot with volumetric micro-computed tomography image guidance for small animal stereotactic interventions," *Med. Phys.*, 37(4), 1647-1659, 2010.
- [40] A.C. Waspe, *Development of a Robotic Needle Positioning System for Three-Dimensional Image-Guided Interventions in Small Animals*, Ph.D. thesis, University of Western Ontario, 2009.
- [41] P. Kazanzides, J. Chang, I. Iordachita, J. Li, C.C. Ling, and G. Fichtinger, "Development of an image-guided robot for small animal research," *Comput. Aided Surg.*, 12(6), 357–365, 2007.
- [42] J. Chang, B. Wen, P. Kazanzides, P. Zanzonico, R.D. Finn, G. Fichtinger and C. C. Ling, "A robotic system for 18F-FMISO PET-guided intratumoral pO₂ measurements," *Med. Phys.*, 36(11), 2009.
- [43] A. Ayadi, G. Bour, M. Aprahamian, B. Bayle, P. Graebbling, J. Gangloff, L. Soler, J.M. Egly and J. Marescaux, "Fully automated image-guided needle insertion: Application to small animal biopsies," *Proc. 29th Int. Conf. IEEE. EMBS. Cité Int.*, 2007, pp. 194 - 197.
- [44] S.A. Nicolau, L. Mendoza-Burgos, L. Soler, D. Mutter and J. Marescaux, "In vivo evaluation of a guidance system for computer assisted robotized needle

insertion devoted to small animals,” *Lect. Notes Comp. Sci.*, 5128, pp. 241-250, 2008.

- [45] L. Ramrath, U.G. Hofmann and A. Schweikard, “A robotic assistant for stereotactic neurosurgery on small animals,” *Int. J. Med. Robot. Comp.* 4(4), 295–303, (2008).
- [46] B.M. Pohl, A. Schumacher and U.G. Hofmann, “Towards an automated, minimal invasive, precision craniotomy on small animals,” *Proc. 5th Int. IEEE. EMBS. Conf. on Neur. Eng.*, 2011, pp. 302-305.
- [47] O. Bebek, M. J. Hwang, B. Fei, and M. C. Cavusoglu, “Design of a small animal biopsy robot,” *Proc. 30th Int. Conf. IEEE EMBS*, 2008, pp. 5601–5604.
- [48] O. Bebek, M. J. Hwang, B. Fei, and M. C. Cavusoglu, “Design of a parallel robot for needle-based interventions on small animals,” *IEEE/ASME Trans. Mecha.*, in press, 2011.
- [49] S.A. Nicolau, L. Goffin and L. Soler, “A low cost and accurate guidance system for laparoscopic surgery: Validation of an abdominal phantom,” *Proceedings of ACM Symposium on Virtual Reality Software and Technology*, 2005, pp. 124-133.
- [50] K. S. Arun, T. S. Huang, and S. D. Blostein, "Least-squares fitting of two 3-D point sets," *IEEE Trans. Pattern Anal. Mach. Intell.* PAMI-9(5), 698–700, 1987.
- [51] P. J. Besl and H. D. McKay, “A method for registration of 3-D shapes,” *IEEE Trans. Pattern Anal. Mach. Intell.*, 14(2), 239–256, 1992.
- [52] J.M. Fitzpatrick and J.B. West, “The distribution of target registration error in rigid-body point-based registration,” *IEEE Trans. Med. Imag*, 20(9), 917-927, 2001.
- [53] J.M. Fitzpatrick, J.B. West and C.R. Maurer, “Predicting error in rigid-body point-based registration,” *IEEE Trans. Med. Imag*, 17(5), 694-702, 1998.

- [54] J.B. West, J.M. Fitzpatrick, S.A. Toms, C.R. Maurer and R.J. Maciunas, "Fiducial point placement and the accuracy of point-based, rigid body registration," *Neurosurgery*, 48(4), 810-817, 2001.
- [55] R.I. Frankel, "Centennial of Röntgens's discovery of X-rays," *Western Journal of Medicine*, 164(6), 497-501, 1995.
- [56] J.A. Siebert and J.M. Boone, "X-ray imaging physics for nuclear medicine technologists. Part 2: X-ray interactions and image formations," *Journal of Nuclear Medicine Technology*, 33(1), 3-18, 2005.
- [57] Hounsfield G N, "Computerized transverse axial scanning (tomography): Part 1. description of system," *Br. J. Rad.*, 46, 1016–1022, 1973.
- [58] M. Mahesh, "Search for isotropic resolution in CT from conventional through multiple-row detector." *Radiographics*, 22(4), 949-962, 2002.
- [59] W.A. Kalender, "X-ray computed tomography", *Phy. Med. Biol*, 51, R29-R43, 2006.
- [60] E.L. Ritman, "Small-animal CT: Its difference from, and impact on, clinical CT," *Nucl. Instr. Meth. Phys. Res. A*, 580, 968-970, 2007.
- [61] J.C. Elliot and S.D. Dover, "X-ray microtomography," *J. Microsc.*, 126(2), 211-213, 1982.
- [62] S.J. Schambach, S. Bag, L. Schilling, C. Groden and M.A. Brockmann, "Application of micro-CT in small animal imaging," *Methods*, 50(1), 2-13, 2010.
- [63] S.H. Bartling, W. Stiller, W. Semmler and F. Kiessing, "Small animal computed tomography imaging," *Curr. Med. Imaging Rev.*, 3(1), 45-59, 2007.

- [64] L. Y. Du, J. Umoh, H. N. Nikolov, S. I. Pollmann, T. Y. Lee and D. W. Holdsworth, "A quality assurance phantom for the performance evaluation of volumetric micro-CT systems," *Phys. Med. Biol.*, 52(23), 7087–7108, 2007.
- [65] M.A. Bahri, G. Warnock, A. Plenevaux, P. Choquet, A. Constantinesco, E. Salmon, A. Luxen and A. Seret, "Performance of the general electric eXplore CT 120 micro-CT using the vmCT phantom," *Nucl. Instr. and Meth A*, in press, 2010.
- [66] E. Perilli, F. Baruffaldi, M.C. Bisi, L. Cristofolini and A. Cappello, "A physical phantom for the calibration of three-dimensional X-ray microtomography examination," *J. Microsc.*, 222(2), 124-134, 2006.

Chapter 2

2 Traceable Micro-CT Geometric Accuracy Phantom for Applications Requiring Exact Measurement of Distances or Volumes

2.1 Introduction

Volumetric x-ray micro-computed tomography (micro-CT) is an increasingly important tool for research requiring imaging of small specimens or animals [1]. The growing importance of micro-CT is reflected in the exponential growth of publications since the early 1980s on the topic of small animal micro-CT imaging and the availability of a variety of micro-CT scanners from at least a dozen manufacturers [2]. Although often used for qualitative research applications, micro-CT has also developed into a useful tool for a wide-range of quantitative applications. Micro-CT has been used for quantitative measurements in small-animal imaging applications such bone volume and roughness [3], tracking of tumor progression and volume [4], and quantification of whole body composition [5]. Micro-CT has been employed for quantitative assessment of medical devices such as characterization of ion chambers [6] and measurement of wear in replacement joints [7]. Micro-CT images have also been used to guide mechatronic devices to complete preclinical micro-injection procedures [8,9]. The success and utility of these applications depends on the geometric fidelity of images produced by micro-CT scanners. In applications that demand the highest geometric fidelity, such as characterization of ion chambers or guidance of devices, the ability to characterize the geometric accuracy of micro-CT scanners to a traceable standard [10] would ensure the highest quality results.

In-plane geometric inaccuracies of 0.2% [11] and 0.3% [12] have been previously reported for micro-CT scanners. These percentages represent the error in calibration of the micro-CT voxel size. The reported errors correspond to an error of 20 to 30 μm per centimeter of distance in an image. Although these errors are relatively small, they can still exert a noticeable negative influence on quantitative results. For instance, micro-CT

image-guided microinjection procedures may require a needle-positioning error of $< 200\ \mu\text{m}$ to reach small targets [8]. The demanding requirements of these procedures challenge the limits of micro-CT scanners. The previously reported geometric inaccuracies of micro-CT scanners would result in an error of approximately $50\ \mu\text{m}$, or at least one fourth of the allowable positioning error, when applied over an insertion distance of 20 mm. Geometric inaccuracies in micro-CT images are an error source that cannot be neglected and should be minimized for such demanding applications.

Previous quality assurance phantoms have only partially addressed the considerations relevant to ensuring the geometric accuracy of micro-CT scanners. Perilli *et al.* developed a phantom consisting of aluminum inserts of known geometry embedded in a cylinder of polymethylmethacrylate to evaluate imaging parameters for trabecular bone imaging applications [13,14]. The known geometries of the inserts were compared to their geometry in the micro-CT images to evaluate the geometric accuracy of the scanner. However, the geometry of the inserts was never qualified to a traceable standard and the phantom did not offer a method to correct detected geometric inaccuracies in images. Du *et al.* developed a quality assurance phantom to assess a number of parameters related to image quality, including geometric accuracy [7]. The phantom assessed geometric accuracy by comparing the known separations of five beads to their positions in micro-CT images. However, again, the bead separations were never qualified to a traceable standard. The phantom also only provided a measurement of in-plane geometric accuracy.

In this paper, a compact quality assurance phantom qualified to a traceable standard is presented along with an automated image processing algorithm to characterize the geometric accuracy of micro-CT scanners and calculate correction factors to reduce the geometric error of images. The phantom and algorithm are used to evaluate the geometric accuracy of five micro-CT scanners representing four different models of micro-CT systems. The calculated correction factors are applied to measurements of fiducial markers in each of the five scanners to evaluate their ability to improve fiducial localization. The techniques developed in this study will allow micro-CT end users to

guarantee the highest level of geometric fidelity and to calibrate images to a traceable standard.

2.2 Methods

2.2.1 Calibration Phantom Construction

A calibration phantom was custom-built to evaluate the geometric accuracy of micro-CT scanners. The physical size of the phantom is approximately 45 mm × 25 mm × 40 mm. The small size of the phantom enables it to be easily integrated onto a mechatronic device and allows it to fit within a wide range of micro-CT bore sizes. The calibration phantom contains six fiducial markers, which are 6.35 mm (¼") diameter borosilicate spherical beads (8996K25, McMaster-Carr, Cleveland, OH). The fiducials are fixed in position using a frame constructed onto a 6.35 mm diameter carbon fiber shaft backbone. Three custom-made Delrin plastic clamps are attached to the carbon fiber backbone. Each of the three clamps supports a 15 mm length of 6.35 mm diameter carbon fiber rod to which the borosilicate bead fiducials are attached using cyanoacrylate glue. A micro-CT surface rendering of the completed calibration phantom is provided in **Figure 2.1**.

The phantom design was carefully developed to ensure the phantom is compact, possesses high dimensional stability, and the fiducials can be easily segmented and their centroid calculated in micro-CT images. Delrin plastic and carbon fiber were selected for frame construction due to their high rigidity and low x-ray attenuation. Rigidity is a key material property since high dimensional stability of bead locations is required; shifts in bead positions would cause overestimation of image geometric error. For the frame, low x-ray attenuation is also a key material property to avoid micro-CT imaging artifacts and ease segmentation and centroiding of the borosilicate beads. The borosilicate beads selected as fiducials possess a precise sphericity of 2.54 µm for the bead diameter. The sphericity of each bead was validated to a traceable standard using gauge blocks (Grade B-18, Mitutoyo Canada Inc., Toronto, ON, Canada) and an indicator (Model 24165-10, Starrett, Waite Park, MN). The high sphericity of the beads ensures accuracy in phantom construction and in centroiding the beads in micro-CT images.

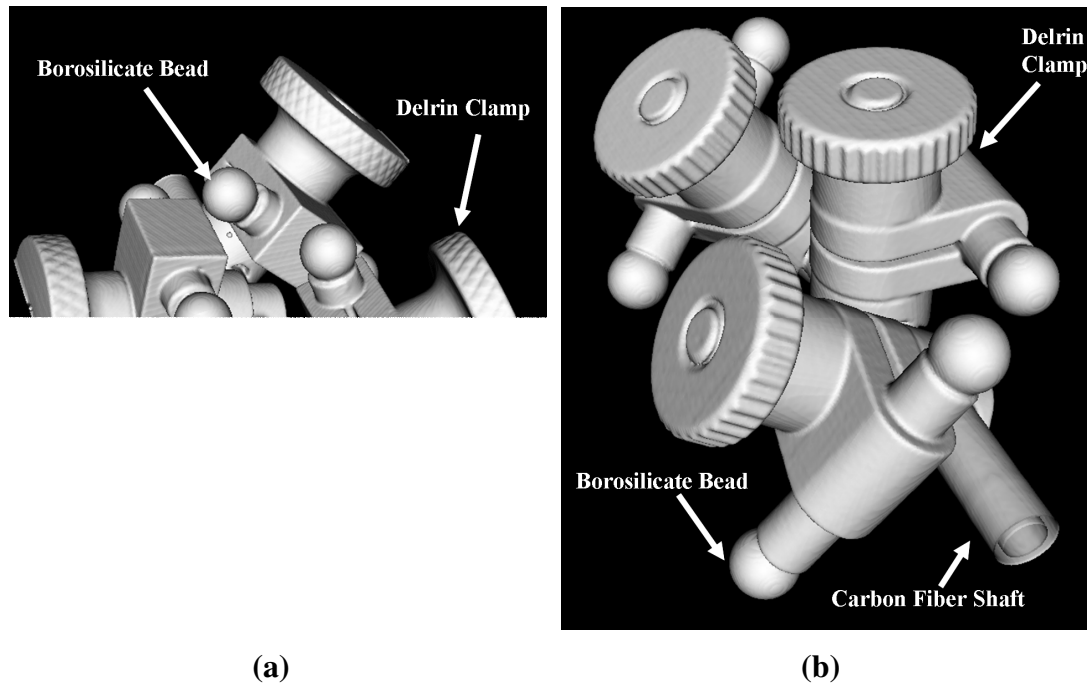


Figure 2.1-Micro-CT surface rendering of the a) calibration phantom and b) validation phantom.

2.2.2 Measurement of Bead Positions within Calibration Phantom

The calibration phantom was used to evaluate the geometric accuracy of micro-CT scanners by comparing the known positions of beads within the phantom to the position of the beads in a micro-CT image. The dimensional accuracy of the calibration phantom is therefore critical to enable detection and correction of geometric errors of $< 1\%$ of the voxel dimensions of micro-CT scanners. Therefore, a method was developed to measure the bead positions to a known and traceable standard.

The position of each bead in the phantom was measured using a calibrated XYZ positioning stage (M-462-XYZ-SD Series, Newport, Irvine, CA) with an attached dial indicator (Model 24165-10, Starrett, Waite Park, MN) mounted onto a granite surface plate (Grade B, Starrett, Waite Park, MN). The phantom was suspended above the granite surface plate by clamping its carbon fiber backbone to a V-block (Model 228, Starrett, Wait Park, MN). Gauge blocks (Grade B-18, Mitutoyo Canada Inc., Toronto, ON, Canada) with certified, traceable dimensional accuracy were stacked onto the granite surface plate. The height of the stacked gauge blocks was compared to the height of a

single bead above the granite surface using the XYZ positioning stage and attached indicator. The height of the gauge blocks was iteratively adjusted until the dial indicator showed no difference between the stack height and bead height. The dial indicator provided a distance resolution of $2.54\text{ }\mu\text{m}$. The distance measurement process was completed for each of the six fiducial beads. The distance of each bead from the granite surface plate was then measured twice more in the two directions orthogonal to the original measurement. The orthogonal distances were measured by rotating the V-block on the granite surface plate and repeating the iterative measurement process for each bead. The orthogonality of the V-block was measured by the same XYZ stage and attached indicator to be $< 2.54\text{ }\mu\text{m}$ over 2.0 cm of travel. The phantom and measurement tools are shown in **Figure 2.2**. Using this method, the three-dimensional position of each bead in the phantom was determined relative to a known and traceable standard of measurement. The mean and standard deviation of the bead separations in the phantom was $24.14 \pm 7.51\text{ mm}$.

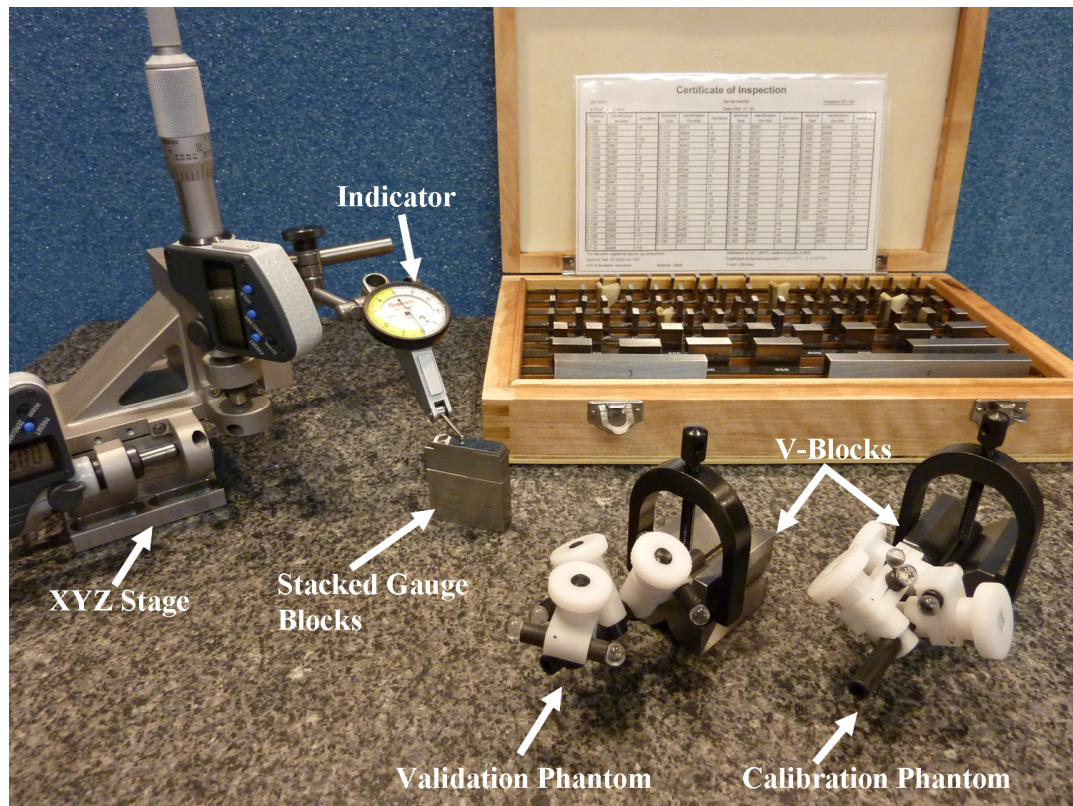


Figure 2.2- Calibration and validation phantom with measurement equipment.

2.2.3 Imaging the Calibration Phantom

The calibration phantom was used to evaluate the geometric accuracy of five volumetric x-ray micro-CT scanners manufactured by General Electric Healthcare Biosciences (London, ON, Canada). The scanners evaluated included two eXplore Ultra Locus scanners and one of each of eXplore speCZT, eXplore CT 120 and eXplore RS scanner models. These scanners represent a range of commercially available micro-CT scanning equipment commonly employed in research laboratories, with a range of voxel spacing (0.05 mm to 0.15 mm) and transaxial field-of-view (70 mm to 150 mm).

A single common calibration phantom was imaged by all five scanners. The calibration phantom was scanned by each scanner five times at the approximate scanner isocenter. The phantom was removed from the micro-CT bore and repositioned between each scan. For both the eXplore Ultra Locus, in addition to five additional scans at the isocenter, five scans were taken at a position offset from the scanner isocenter by approximately 70 mm, for a total of 10 scans. The phantom was not scanned at a second position in the three remaining scanners since it almost fully occupied these scanners' maximum trans axial field-of-view. The imaging parameters used for each scanner are summarized in **Table 2.1**.

Table 2.1-Summary of the micro-CT scan parameters used for imaging the phantoms.

Scanner	Tube Voltage (kVp)	Tube Current (mA)	Views	View Exposure Time (ms)	Total Scan Time	Nominal Voxel Size (μm)
eXplore Locus Ultra	140	20	1000	16	16 seconds	153.9
eXplore SpecZT	110	32	900	16	5 minutes	49.8
eXplore CT 120	110	32	900	16	5 minutes	49.7
eXplore RS	80	45	900	400	120 minutes	45.4

2.2.4 Geometric Correction Calculation

An automated algorithm was developed using MATLAB (The Mathworks, Inc., Natick, MA) to compare the known position of beads in the phantom to their positions in the micro-CT images. The algorithm determines the position of the phantom's borosilicate beads in the images by using a multi-step localization technique. Beads were first segmented using a threshold-based region growing algorithm. The threshold level was calculated using an iterative algorithm to determine the threshold that yielded an average segmented volume of the beads to within 0.1% of the known volume. The center of the segmented bead was then calculated using a squared-intensity-weighted centroiding algorithm that has an accuracy of < 5% of the nominal image voxel size in localizing 3D centroid positions in simulated images [15]. Since distance is measured between pairs of bead centroids, the worst-case distance error is double the centroiding error.

The distance of each bead to all other beads in the phantom was measured for a total of 15 distances per image. The 3D separation of each pair of beads in the image was scaled to the known bead separations using the equation:

$$Dist_{Known} = \sqrt{(X_{img}/CF_x)^2 + (Y_{img}/CF_y)^2 + (Z_{img}/CF_z)^2} \quad (2.1)$$

where X_{img} , Y_{img} , and Z_{img} are the components of the bead distance in the images along the respective axes of the scanner and CF_x , CF_y , and CF_z are correction factors for each scanner axis that transform the bead separations in the images to the known bead separations. **Equation 2.1** for each of the 15 bead distances was combined to form the system of equations:

$$\begin{bmatrix} X_{img1}^2 & Y_{img1}^2 & Z_{img1}^2 \\ \downarrow & \downarrow & \downarrow \\ X_{img15}^2 & Y_{img15}^2 & Z_{img15}^2 \end{bmatrix} \times \begin{bmatrix} (1/CF_x)^2 \\ (1/CF_y)^2 \\ (1/CF_z)^2 \end{bmatrix} = \begin{bmatrix} Dist_{known1}^2 \\ \downarrow \\ Dist_{known15}^2 \end{bmatrix} \quad (2.2)$$

The least-squares solution of **Equation 2.2** was determined to calculate values for each of the correction factors.

2.2.5 Validation Phantom Construction

A second phantom was constructed to validate the correction factors measured by the calibration phantom. The validation phantom is an independent verification that the calculated correction factors are not unique to the calibration phantom and generally correct images produced by the micro-CT scanner. The validation phantom, like the calibration phantom, contains six 6.35 mm (1/4") diameter borosilicate spherical beads acting as fiducial markers that are secured to a 6.35 mm diameter carbon fiber shaft backbone using Delrin clamps. The positions of the beads in the validation phantom differed from the bead positions in the calibration phantom. Different bead positions were obtained by changing the angle of the Delrin clamps relative to the phantom backbone and by increasing the lengths of carbon fiber rods used to mount the beads to 25.4 mm. Once the validation phantom was constructed, the bead positions within the phantom were measured using the method described in **Section 2.2.2**. A micro-CT surface rendering of the validation phantom is shown in **Figure 2.1**. The mean and standard deviation separation between the pairs of beads was 39.41 ± 12.99 mm

A rigid-body registration was computed between the measured bead positions of the calibration and validation phantoms. The registration was calculated to ensure that the bead positions in the validation phantom were truly independent of the calibration phantom. A large rigid-body registration, as demonstrated by a large fiducial registration error (FRE) [16], would indicate that the validation phantom bead arrangement was different from the calibration phantom arrangement. An FRE > 6.35 mm (or approximately one bead diameter) was assumed to indicate a sufficiently different bead arrangement. The smallest FRE of the rigid body registration of the measured calibration bead locations to the validation phantom bead locations was 18.4 ± 6.3 mm, or approximately three fiducial bead diameters.

The validation phantom was imaged once at the isocenter of each scanner. Again for both the eXplore Ultra Locus scanners, the phantom was imaged at an additional position offset from the isocenter. For each scanner, the same scan parameters (**Table 2.1**) were used for the validation phantom. The validation phantom beads were segmented and centroided using the algorithm described in **Section 2.2.4**. The distances

between each bead pair in the validation phantom was calculated with and without applying the correction factors calculated for each scanner using the calibration phantom.

2.2.6 Data Analysis

The three correction factors for each scanner were compared using ANOVA and Tukey tests at a significance level at $p < 0.05$ to determine if any statistically significant differences exist for the correction factors along the X, Y and Z axes of each scanner. This comparison was performed to determine if the geometric error of each scanner was isotropic or anisotropic. If the correction factors are not significantly different (i.e. indicating an isotropic error) a single averaged correction factor could be used for each axis. For the two eXplore Locus Ultra scanners, pairs of correction factors from the isocenter and offset position for each axis were compared using a two-tailed paired t-test with $p < 0.05$ to determine if any significant difference exists for each respective correction factor at the two positions. If correction factors from the two positions are significantly different, it may indicate that the values of the correction factors are dependent on position within the scanner bore.

The effectiveness of the correction factors for improving the geometric accuracy of micro-CT scanners was also evaluated. The separations among beads within the calibration and validation phantoms were calculated with and without using the correction factors. For each bead separation in each image, the geometric error was determined using the gauge block measurements as a gold standard. The error of the uncompensated and corrected separations was compared using a two-tailed paired t-test at $p < 0.05$ to determine if the correction factors significantly reduced the error. Reductions in the error of the bead separations in the images that are both statistically significant and large enough to be practically meaningful would demonstrate the efficacy of the geometric correction procedure.

Table 2.2- Calculated average scanner correction factors for each axis.

Scanner	X-Axis Correction Factor	Y-Axis Correction Factor	Z-Axis Correction Factor	Volumetric Correction Factor
eXplore Locus Ultra Isocenter Scanner One	0.9998 ± 0.00006	1.0009 ± 0.00012	1.0002 ± 0.00021	1.0008 ± 0.00034
eXplore Locus Ultra Offset Scanner One	1.0008 ± 0.00063	0.9968 ± 0.00018	0.9987 ± 0.00040	0.9962 ± 0.00063
eXplore Locus Ultra Isocenter Scanner Two	1.0033 ± 0.00013	0.9981 ± 0.00012	0.9978 ± 0.00014	1.0020 ± 0.00012
eXplore Locus Ultra Offset Scanner Two	1.0022 ± 0.00010	0.9999 ± 0.00009	0.9998 ± 0.00008	0.9993 ± 0.00012
eXplore SpecZT	1.0011 ± 0.00007	1.0008 ± 0.00002	0.9990 ± 0.00004	1.0009 ± 0.00043
eXplore CT 120	1.0027 ± 0.00006	1.0031 ± 0.00103	1.0005 ± 0.00014	1.0064 ± 0.00133
eXplore RS	0.9963 ± 0.00021	0.9965 ± 0.00069	0.9957 ± 0.00025	0.9886 ± 0.00092

The eXplore CT 120, eXplore specCZT and eXplore RS all yielded images with a voxel size of approximately 50 μm . The corrected and uncorrected errors of these three scanners were compared using ANOVA and Tukey tests with $p < 0.05$ to see if errors were consistent across three scanners with images of similar voxel sizes. Finally, the corrected and uncorrected errors of the two positions of the two eXplore Locus Ultra scanners were also compared using a two-tailed paired t-test to determine if scanners of the same model possess similar errors.

2.3 Results

2.3.1 Correction Factor Values

The mean and standard deviation of the correction factors for each axis of each scanner is summarized in **Table 2.2**. In addition, an average volumetric correction factor is provided to characterize the correction in voxel volume for each scanner arising from the linear axis correction factors. A correction factor > 1 indicates that distances in the uncorrected micro-CT images overestimated the true dimensions. There was no clear pattern to the magnitudes or directions (over or under estimation) of the errors along the

Table 2.3-Results of Tukey test ($p < 0.05$) for differences in the mean correction factors for each pair of scanner axes.

Scanner	X and Y	X and Z	Y and Z
eXplore Locus Ultra Isocenter Scanner One	Yes	No	Yes
eXplore Locus Ultra Offset Scanner One	Yes	Yes	No
eXplore Locus Ultra Isocentre Scanner Two	Yes	Yes	Yes
eXplore Locus Ultra Offset Scanner Two	Yes	Yes	Yes
eXplore SpecZT	No	Yes	Yes
eXplore CT 120	No	Yes	Yes
eXplore RS	No	No	Yes

three axes. A statistically significant difference was found between the correction factors in the X ($p = 0.043$ and $p < 0.001$), Y ($p < 0.001$ for both scanners) and Z ($p < 0.001$ for both scanners) axes at the two bore positions in both eXplore Locus Ultra scanners. These results suggest that the calibration phantom should ideally be placed as close as possible in the bore to the anticipated location of targets.

The results of Tukey tests comparing the correction factors for each scanner are summarized in **Table 2.3**. For three out of four scanner models, no significant difference was found between the X and Y correction factors for the scanners, indicating a single average correction factor can be used for the in-plane direction. The X and Y correction factors were significantly different for the two eXplore Locus Ultra scanners. However, for these two scanners the absolute difference was still $< 1\%$. In 11 out of 14 cases, the X and Y correction factors were generally significantly different from the Z correction

Table 2.4-Uncorrected and corrected bead separation errors for the calibration phantom. Each error is described with a mean and standard deviation in both an absolute value of μm and as a percent of total bead separation. The p-value of the t-tests comparing the corrected and uncorrected errors of each scanner are provided.

Scanner	Uncorrected Error (μm)	Corrected Error (μm)	Uncorrected Error (%)	Corrected Error (%)	p-Value
eXplore Locus Ultra Isocenter Scanner One	22 ± 2	22 ± 3	0.096 ± 0.013	0.101 ± 0.016	$p = 0.03$
eXplore Locus Ultra Offset Scanner One	38 ± 3	31 ± 4	0.172 ± 0.014	0.148 ± 0.014	$p = 0.002$
eXplore Locus Ultra Isocentre Scanner Two	19 ± 1	7 ± 1	0.078 ± 0.006	0.031 ± 0.007	$p < 0.001$
eXplore Locus Ultra Offset Scanner Two	36 ± 1	35 ± 1	0.146 ± 0.003	0.150 ± 0.003	$p = 0.16$
eXplore SpecZT	18 ± 4	11 ± 3	0.080 ± 0.016	0.054 ± 0.014	$p < 0.001$
Explore CT 120	50 ± 7	7 ± 1	0.200 ± 0.027	0.007 ± 0.001	$p = 0.001$
eXplore RS	92 ± 6	9 ± 2	0.380 ± 0.027	0.042 ± 0.011	$p < 0.001$

factors, which suggest the out-of-plane correction factor is unique from the in-plane correction factors.

2.3.2 Geometric Correction to Calibration Phantom

The corrected and uncorrected bead separations within the calibration phantom are summarized in **Table 2.4**. Application of the correction factors significantly reduced the error in bead separations for in five out of seven image sets. In six out of the seven image sets, the corrected and uncorrected errors were found to be significantly different. The mean difference in corrected and uncorrected errors ranged from $\leq 1 \mu\text{m}$ to $83 \mu\text{m}$ in absolute terms or from 0.005% to 0.338% in relative terms.

Table 2.5-Uncorrected and corrected bead separation errors for the validation phantom. Each error is described with a mean and standard deviation in both an absolute value of μm and as a percent of total bead separation. The p-value of the t-tests comparing the corrected and uncorrected errors of each scanner are provided.

Scanner	Uncorrected Error (μm)	Corrected Error (μm)	Uncorrected Error (%)	Corrected Error (%)	p-Value
eXplore Locus Ultra Isocenter Scanner One	37 ± 27	38 ± 26	0.100 ± 0.080	0.101 ± 0.074	$p=0.46$
eXplore Locus Ultra Offset Scanner One	44 ± 36	54 ± 41	0.132 ± 0.138	0.163 ± 0.158	$p=0.26$
eXplore Locus Ultra Isocentre Scanner Two	27 ± 15	29 ± 15	0.077 ± 0.068	0.084 ± 0.056	$p=0.69$
eXplore Locus Ultra Offset Scanner Two	44 ± 22	80 ± 54	0.132 ± 0.117	0.215 ± 0.145	$p=0.01$
eXplore SpecZT	15 ± 10	19 ± 13	0.047 ± 0.041	0.049 ± 0.033	$p=0.35$
eXplore CT 120	67 ± 27	22 ± 16	0.168 ± 0.037	0.052 ± 0.025	$p<0.001$
eXplore RS	148 ± 61	27 ± 19	0.370 ± 0.086	0.074 ± 0.054	$p<0.001$

2.3.3 Geometric Correction to Validation Phantom

The average error in bead separation within the validation phantom for all sets of images was calculated with and without application of the correction factors calculated from the calibration phantom. The corrected and uncorrected bead separations and the p-values for the two-tailed t-tests between the corrected and uncorrected errors are summarized in **Table 2.5**. In three scanners with minimal ($< 50 \mu\text{m}$) geometric accuracy errors, application of the correction factors slightly increased the geometric errors of the images. However, this increase was not statistically significant except for the offset position of the second eXplore Locus Ultra scanner. For the two scanners with $> 60 \mu\text{m}$ uncorrected error, application of the correction factors significantly improved the geometric accuracy of the images.

2.3.4 Comparison of Validation Phantom Errors

The eXplore CT 120, eXplore speCZT and eXplore RS all yielded images with a voxel size of approximately 50 μm . The uncorrected errors of all three scanners were significantly different, but, the corrected errors of the three scanners were not significantly different. This result indicates scanners will possess similar accuracies when corrected by the phantom. The uncorrected errors for each of the two eXplore Locus Ultra scanners were not significantly different from each other at both the isocenter ($p = 0.29$) and offset ($p = 0.94$) positions. Similarly, the corrected isocenter ($p = 0.23$) and offset ($p = 0.21$) positions of each of the two eXplore Locus Ultra scanners were also not significantly different from each other.

2.4 Discussion

We have designed and demonstrated the use of a specialized calibration phantom to measure and correct the geometric accuracy of five different micro-CT scanners spanning four model types. The calibration phantom can be used to calculate traceable correction factors that improve the localization of fiducials in micro-CT images whose positions are independent of the initial calibration phantom.

In two of the five scanners tested, the eXplore CT 120 and eXplore RS, application of the correction factors significantly improved fiducial localization. For these two scanners, the mean geometric error of the images measured by the calibration phantom was reduced from 0.20% and 0.38% to 0.01% and 0.04% respectively. Although the reduction in geometric error is small in absolute terms, the correction factors can provide a significant and meaningful improvement for completing image-guided micro-injection procedures. For the worst-case scanner, the mean error in fiducial localization for the validation phantom was reduced from 0.370% of the bead separation to 0.074% of bead separation. Over a 20 mm distance that a typical small-animal needle positioning device may travel, this represents a reduction of error from 74 to 15 μm . An improvement of 59 μm provides a considerable benefit towards achieving a desirable positioning error $< 200 \mu\text{m}$ for a mechatronic device. In addition, the linear correction factors of each scanner axis multiply to produce a larger volumetric correction. The

greatest volumetric correction was obtained for the eXplore RS and was approximately 1.14%. These results suggest measurement, and if need be, correction of the geometric inaccuracies in micro-CT images may be beneficial for image-guided interventions or other applications that demand high geometric fidelity of images.

The small size of the calibration phantom allows it to fit within the bore of a wide range of micro-CT scanners and to be easily incorporated into the designs of mechatronic devices. The use of an automated algorithm allows the correction factors to be calculated quickly. The most significant interruption to the work flow of mechatronic micro-injection procedures would be the time required to scan and reconstruct images of the calibration phantom. However, micro-CT mechatronic devices typically require a scan at the start of interventions to register the device with the micro-CT scanner. Measurement and correction of scanner geometric inaccuracies could be incorporated into the registration process of mechatronic devices and would only minimally increase the time required for registration. The end user is then assured that localization errors resulting from geometric errors have been minimized and will not impact on the success of their interventions. Calculation and application of geometric correction factors should therefore be incorporated into all procedures using a micro-CT guided mechatronic device.

Statistical analysis of the correction factors suggests the geometric inaccuracy of micro-CT scanners can be slightly anisotropic in nature. Although the observed anisotropy was statistically significant, it was extremely small. The largest percent difference between the mean scaling factors of an axis of a scanner was approximately 0.5% for the isocenter of the second eXplore Locus Ultra scanner. The X and Y correction factors were generally not significantly different from each other but were generally significantly different from the Z correction factor. These results are not surprising. In the scanners tested, the same x-ray detector pixel spacing is used for measurement of the in-plane direction along the X and Y axes but not along the Z axes. These results suggest a single averaged value of the X and Y correction factors can be used along these axes. When exceptions existed for this trend, the absolute difference between these two correction factors remained quite small ($< 0.5\%$), suggesting an

average correction factor can still be used. Between the isocenter and offset positions of the two eXplore Locus Ultra scanners a significant difference in correction factors was found along all three axes. These results suggest the geometric accuracy of micro-CT scanners may vary with location in the bore. The calibration phantom should therefore be placed as near targets as possible.

Interesting inferences can be made from the calculated corrected and uncorrected errors across the micro-CT scanners. The eXplore CT 120, eXplore speCZT and eXplore RS all yielded images with an isotropic voxel size of approximately 50 μm . The eXplore speCZT had a small geometric error indicating it was already well-calibrated for geometric accuracy. Whereas, the eXplore CT 120 and eXplore RS possessed correctable initial geometric errors. A Tukey test found these three scanners to have statistically significant difference in uncorrected errors. However, the corrected errors of these three scanners were not significantly different and are all approximately the same. These results suggest use of the calibration phantom can correct the geometric accuracy of poorly calibrated micro-CT scanners to correspond with the accuracy of an already well calibrated scanner of equivalent voxel size. Similarly, both eXplore Locus Ultra scanners were well calibrated and possessed a similar small geometric error. Between these two scanners, no significant difference was found between the uncorrected and corrected errors. The eXplore Locus Ultra results again suggest scanners of the same voxel size will possess similar geometric errors when calibrated.

Previous studies have measured in-plane geometric errors similar to those reported here for both the eXplore Locus Ultra and eXplore CT 120. Du *et al.* [11] reported a 0.2% error for the eXplore Locus Ultra, which comparable to the $0.10 \pm 0.01\%$ and $0.08 \pm 0.01\%$ errors detected by our calibration phantom at the isocenter of the Locus Ultra and $0.17 \pm 0.01\%$ and $0.15 \pm 0.01\%$ errors detected offset from the isocenter. Bahri *et al.* [12] reported a 0.3% error for the eXplore CT 120, which is comparable to the $0.20 \pm 0.03\%$ error detected using our calibration phantom. Consistent with these previously reported results, our phantom found both the eXplore Locus Ultra and eXplore CT 120 to yield undersized voxels compared to the manufacturer's specification.

2.5 Conclusion

We have designed and developed a traceable calibration phantom and a technique to evaluate the geometric accuracy of micro-CT scanners. The geometric errors detected by this new phantom are in-line with the previous errors reported using non-traceable phantom designs. In two of the five scanners evaluated using the new phantom design, statistically significant correction factors were derived to improve the scanner geometric accuracy. However, for many applications, the impact of these correction factors would be small. These results suggest that a non-traceable phantom design is sufficient for the geometric calibration of micro-CT scanners for the majority of applications. Use of a traceable calibration phantom may be useful for applications demanding the very highest geometric fidelity of images, such as small animal image-guided interventions or the characterization of medical devices. In any case, the use of a geometric calibration phantom, traceable or not, is an easily implemented assurance to micro-CT end users of the geometric fidelity of their images.

References

- [1] C.T. Badea, M. Drangova, D.W. Holdsworth and G.A. Johnson, "In vivo small-animal imaging using micro-CT and digital subtraction angiography," *Phys. Med. Biol.*, 53(19), R319-350, 2008.
- [2] S.J. Schambach, S. Bag, L. Schilling C. Groden and M.A. Brockmann, "Application of micro-CT in small animal imaging," *Methods*, 50(1), 2-13, 2010.
- [3] M.D. Silva, A. Savinainen, R. Kapadia, J. Ruan, E. Siebert, N. Avitahl, R. Mosher, K. Anderson, B. Jaffee, L. Schopf and S. Chandra, "Quantitative analysis of micro-CT imaging and histopathology signatures of experimental arthritis in rats," *Mol. Imag.*, 3(3), 312-318, 2004.
- [4] E. Namati, J. Theisse, J.C. Sieren, A. Ross, E. A. Hoffman and G. McLennan, "Longitudinal assessment of lung cancer progression in the mouse using in-vivo micro-CT imaging," *Med. Phys.* 37(9), 4793-4805, 2010.
- [5] P.V. Granton, C. J. D. Norley, J. Umoh, E. A. Turley, B.C. Frier, E.G. Noble and D.W. Holdsworth, "Rapid in vivo whole body composition of rats using cone beam μ CT," *J. Appl. Physiol.*, 109, 1162-1169, 2010.
- [6] A.L. McNiven, J. Umoh, T. Kron, D.W. Holdsworth and J.J. Battista, "Ionization chamber volume determination and quality assurance using micro-CT imaging," *Phys. Med. Biol.* 53(18), 5029-5043 (2008).
- [7] M.G. Teeter, D.D. Naudie, D.D. McErlain, J.M. Brandt, X. Yuan, S.J. Macdonald and D.W. Holdsworth, "In vitro quantification of wear in tibial inserts using microcomputed tomography," *Clin. Orthop. Relat. Res.* 469(1), 107-112 2010.
- [8] S.A. Nicolau, L. Mendoza-Burgos, L. Soler, D. Mutter and J. Marescaux "In vivo evaluation of a guidance system for computer assisted robotized needle insertion devoted to small animals," *Lect. Notes Comp. Sci.*, 5128, 241-250, 2008.

- [9] A.C. Waspe, D.D. McErlain, V. Pitelka, D.W. Holdsworth, J.C. Lacfield and A. Fenster "Integration and evaluation of a needle positioning robot with volumetric micro-computed tomography image guidance for small animal stereotactic interventions," *Med. Phys.*, 37(4), 1647-1659, 2010.
- [10] C.K. Ross, "Comments on 'Ionization chamber volume determination and quality assurance using micro-CT imaging'," *Phys. Med. Biol.* 54(6), L23-27; author reply L29-30 (2009).
- [11] L. Y. Du, J. Umoh, H. N. Nikolov, S. I. Pollmann, T. Y. Lee and D. W. Holdsworth, "A quality assurance phantom for the performance evaluation of volumetric micro-CT systems," *Phys. Med. Biol.*, 52(23), 7087–7108, 2007.
- [12] M.A. Bahri, G. Warnock, A. Plenevaux, P. Choquet, A. Constantinesco, E. Salmon, A. Luxen and A. Seret, "Performance of the General Electric eXplore CT 120 micro-CT using the vmCT phantom," *Nucl. Instr. and Meth A*, in press, 2010.
- [13] E. Perilli, F. Baruffaldi, M.C. Bisi, L. Cristofolini and A. Cappello, "A physical phantom for the calibration of three-dimensional X-ray microtomography examination," *J. Microsc.*, 222(2), 124-134, 2006.
- [14] R. Stoico, S. Tassani, E. Perilli, F. Baruffaldi and M. Viceconti, "Quality control protocol for in vitro micro-computed tomography," *J. Microsc.*, 238(2), 162-172, 2010.
- [15] A. Patwardhan, "Subpixel position measurement using 1D, 2D and 3D centroid algorithms with emphasis on applications in confocal microscopy," *J. Microsc.*, 186(3), 246–247, 1997.
- [16] J. M.Fitzpatrick, J.B. West and C.R. Maurer Jr., "Predicting error in rigid-body point-based registration," *IEEE Trans. Med. Imaging* , (17)5, 694-702, 1998.

Chapter 3

3 3D Image-Guided Robotic Needle Positioning System for Small Animal Interventions

3.1 Introduction

Clinical medical robotics is a mature field and dozens of clinical robotic systems have been developed for use in a wide range of interventional applications [1]. Today, use of medical robotics is increasingly becoming part of routine procedures; for example, the da Vinci robot by Intuitive Surgical for radical prostatectomy [2]. This growing use and importance of medical robotic systems is a stark contrast to the state of robotics for use with small animals in preclinical research. A particular preclinical application, which could greatly benefit from the use of robotics, is the development of an image-guided robotic system for needle interventions. Although a number of systems have been developed for image-guided clinical needle interventions [3]; no such systems are in use for routine preclinical use. Rather, sub-optimal non-robotic and non-image-guided techniques remain the norm for small animal needle interventions. Techniques typically used for small animal needle interventions require surgical exposure of targets [4-7], percutaneous injections through the skin [4,8] or stereotactic devices [9]. Surgical exposure suffers from associated surgical mortality and morbidity, which may confound research results. Both percutaneous and surgical techniques are, ultimately, highly dependent on the ability of a human operator to correctly place a needle and suffer from problems of accuracy and repeatability. Stereotactic devices are limited to interventions within the skull and are limited by the accuracy of anatomic atlases and localization of external landmarks. The current methods typically used for small animal needle interventions are relatively unsophisticated in comparison to clinical methods.

Imaging technology has outperformed robotics in the development of specialized small-animal systems for preclinical research. Analogous small-animal imaging systems have been developed for all the major clinical imaging modalities including: Computed Tomography (CT), Magnetic Resonance (MR), Positron Emission Tomography (PET), Single-Photon Emission Computed Tomography (SPECT) and Ultrasound. These small-

animal imaging systems have achieved popular use and are considered to have greatly contributed to preclinical research [10]. CT imaging developed for use with small-animals, commonly referred to as micro-CT, is a particular imaging modality of interest. Micro-CT scanners are available from at least a dozen manufactures [11] with typical voxel sizes ranging from 5 μm to 450 μm and trans-axial fields of view ranging from 1 to 20 cm [12, 13].

To ameliorate small animal needle interventions, a number of previous efforts have been made to integrate robotic devices with micro-CT imaging systems to perform image-guided needle interventions [14-17]. In addition, several devices not explicitly intended for imaging-guidance have also been developed for small needle interventions and could be potentially integrated with micro-CT imaging [18,19]. The development of these systems combines the accurate and non-invasive target localization of imaging with the positioning accuracy and repeatability of robotic systems. The design requirements that these devices must satisfy are demanding. A needle positioning error of $< 200 \mu\text{m}$ may be required to successfully complete small animal needle interventions [17]. Furthermore, the design of these devices must be extremely compact to allow them to be fully integrated into the small bores of micro-CT imaging systems.

Five previous efforts for potential small animal micro-CT robotic needle intervention systems have been identified. Unfortunately, none of these systems are ideal. The system developed by Waspe *et al.* [17] is the most sophisticated and best characterized of these devices. The system was successfully integrated with a micro-CT scanner and achieved a mean targeting error of $154 \pm 113 \mu\text{m}$ in a tissue mimicking phantom. The system was also able to successfully inject tungsten beads into a rat brain. However, the system was too large to fit within a micro-CT bore and required transport of the animal to the robot workspace following imaging. The system also suffered from variations in targeting accuracy as evident by the large standard deviation in targeting error. The four remaining systems also suffer from a number of drawbacks. The three systems developed by Kazanzides *et al.* [14], Hwang *et al.* [18] and Ramrath *et al.* [19] all lack a demonstrated technique to register the robotic devices with a micro-CT imaging system. The accuracy of these three systems was only evaluated in air rather than using

tissue mimicking phantoms. Ramrath *et al.* achieved an impressive mean positioning accuracy of 32 μm ; however, the robot is based on a stereotactic device and is limited to interventions in the skull. Kazantzides *et al.* and Hwang *et al.* achieved poorer mean targeting accuracies of 0.4 mm and 2 mm respectively. The fourth system developed by Nicolau *et al.* [15] did not have its overall targeting accuracy characterized, but the authors demonstrated the ability to localize the needle tip to within 0.7 mm. None of the aforementioned authors evaluated the ability of their robot to operate within a micro-CT bore.

This paper presents the design of a micro-CT guided small animal robotic needle positioning system and demonstrates the ability to perform needle interventions within the bore of the scanner with a targeting accuracy of $< 200 \mu\text{m}$. The robotic system implements a spherical linkage design, based on the miniaturization of previous clinical systems used for prostate [20] and breast biopsy [21]. The spherical linkages of the robot are designed to create a Remote Center of Motion (RCM) [22]. In order to simplify the robotic design and maintain a small targeting error, a novel implementation of the RCM is used in the system. The positioning error of the robotic system is quantified using targeting experiments in tissue mimicking phantoms. *In vivo* experiments were performed to test the robotic system's ability to direct a needle to a specified target in a xenograft mouse model and to assist with tumour interstitial fluid pressure (IFP) under image guidance.

3.2 Methods

3.2.1 Mechatronic System Design

3.2.1.1 Kinematic Frame Design

High rigidity is the critical factor in the success of a kinematic frame design used for high targeting accuracy. The rigidity of the kinematic frame can be most easily improved by miniaturizing the size of the mechanism. Decreasing the size of the frame by half would increase its rigidity by eight times. In addition, a smaller frame will also allow the robotic system to operate within a micro-CT bore and complete interventions without the need to relocate the animal. Not requiring relocation of the animal during

interventions reduces opportunities for target motion and improves targeting accuracy. The kinematic frame design must therefore be as compact as possible.

The use of a robot architecture based on a fixed remote center of motion (RCM) is best suited for completing a specific task in a confined workspace [1]. The RCM architecture is well established within clinical robotic systems [22]. In a RCM based robot architecture all of the rotational axes of the robot intersect at a common point in 3D space. This architecture allows for higher angular mobility in a confined space such as a scanner bore. An RCM design also has the added advantage of allowing needle translation and orientation to be decoupled when positioning the needle for interventions. The decoupling of translation and orientation no longer makes it necessary to simultaneously control multiple degrees of freedom during the most delicate part of procedures: needle insertion.

A comparative analysis was performed to determine the RCM architecture best-suited for the kinematic frame. The designs considered were: the double parallelogram linkage [17], the goniometric arc [19] and the spherical linkage [18,20]. The double-parallelogram design was found to be unsuitable for this application because of its size and number of components required. The goniometric arc is a simpler design than the double-parallelogram. However, it is difficult to manufacture a linear bearing from CT compatible materials to support the tool in a goniometric arc design. The ferrous materials typically used in most linear bearings will generate streak artifacts because of high attenuation and non-ferrous CT compatible materials typically lack rigidity, which results in bearing deflection and friction. The spherical linkage was found to be advantageous over the other two options due to its simplicity of design. The spherical linkage design also allows for ease in adjustability and calibration to create a precise RCM independent of the manufacturing tolerances in each part of the linkage. The RCM adjustment is accomplished by splitting the base link (**Figure 3.1**) into two parts to control the orientation of each hinged connection in the linkage. The orientation of the hinged connections can then be calibrated to intersect at the RCM. A spherical linkage was selected for the kinematic frame of the system due to its simplicity and ability to achieve a precise RCM.

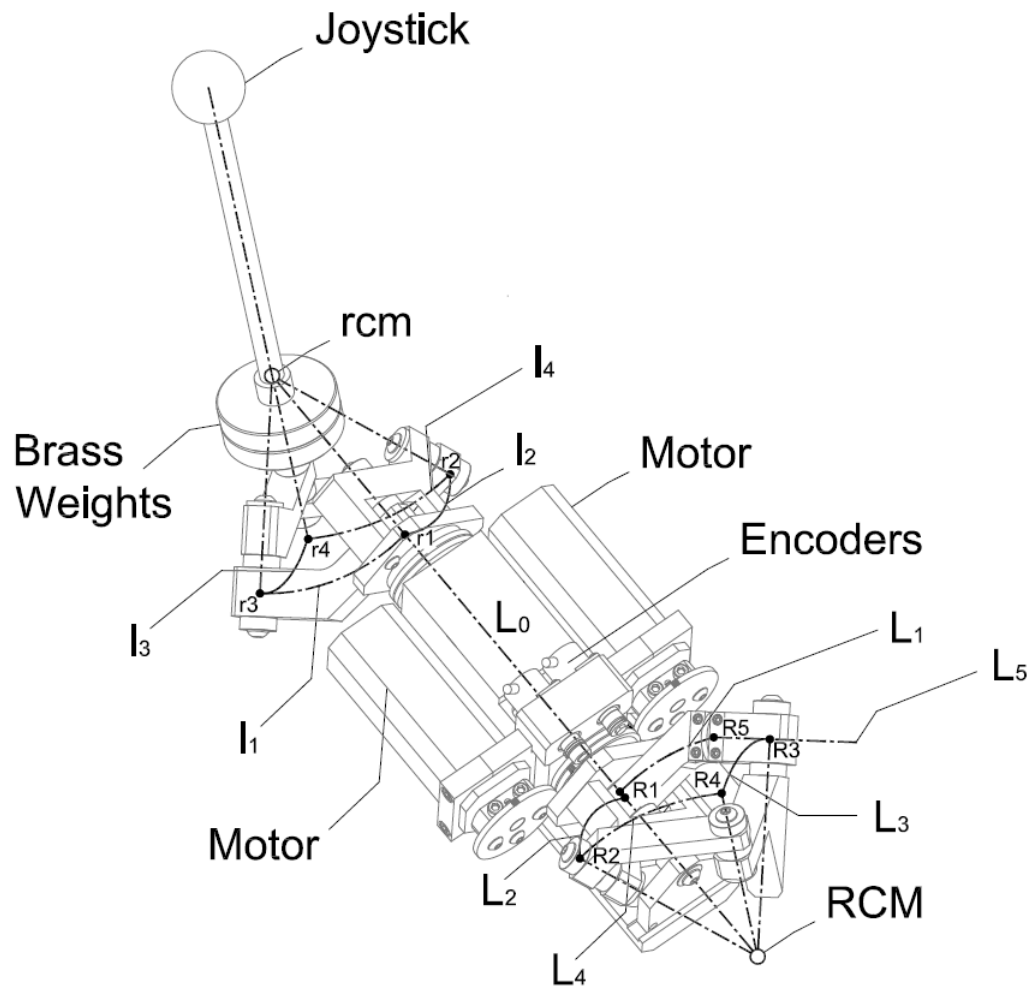


Figure 3.1- A schematic representation of the proposed RCM linkage design which consists of two parts: a forward (labeled L1 through L5) and a rear spherical linkage (labeled I1-I4). The forward spherical linkage consists of five links (L1-L5) supporting the needle driver and five hinged connections (R1-R5) pinned to the base (L0). The rear linkage is a mirror image of the forward linkage and consists of four linkage elements (I1-I5) and four hinged connections (r1-r4). The extra pinned connection (R5) in the forward assembly is used to adjust the axis of each pinned connection (R3 and R4) in the base link (L1 and L5) to create a precise RCM. The linkage functions as a pantograph to constrain the rear linkage to counterbalance the forward linkage and payload using the brass weights attached to the rear spherical linkage. The two encoders are mounted to the base (L0), and record the angle of each rotational axis. The needle is mounted to the link L3 and its axis is aligned along the rotational axis R5. The spherical linkages can be manipulated using either motors or through manual manipulation of a handle mounted to the rear spherical linkage. The axis of each hinged connection in the spherical linkages converges to a common point in space from a remote center of motion: (RCM) at the forward spherical linkage and (rcm) at the rear linkage

3.2.1.2 Mechatronic System Description

The mechatronic system contains a total of 6 degrees of freedom. Two degrees of freedom are contained within the systems spherical linkages, which form two rotational axes: roll and pitch. The rotational axes control needle orientation during interventions. Three degrees of freedom are contained in a custom-built 3-axis XYZ linear stage, which supports the spherical linkage (**Figure 3.2**). The linear stage controls needle translation during interventions. The stage provides 3 cm of stroke along the X and Y axes and 1.5 cm along the Z-axis with an accuracy 2.54 μm in each axis. The position of the stage along each axis is tracked using three optical encoders. Finally, the system consists of a one degree of freedom linear needle driver. The needle driver is used to insert and retract the needle during interventions. Both the mouse bed and robotic system are secured directly to the couch of the micro-CT scanner (**Figure 3.2**). The entire system is compact enough to operate entirely within the micro-CT bore.

The spherical linkage assembly consists of two parts: a forward and a rear linkage (**Figure 3.1**). The forward and rear linkages are coupled together through an elongated shaft assembly. The shaft assembly and associated linkage functions as a pantograph to allow the rear linkage to counterbalance the forward linkage and payload. The forward spherical linkage contains an encoder (RM22SC001 2B30F1C00, Renishaw, Gloucestershire U.K.) for each of the two rotational axes. The two encoders are mounted to the base of the spherical linkage and record the angle of each rotational axis. The encoders allow for real-time monitoring and display of each rotational axes angle. The spherical linkages can be manipulated using either motors or through manual manipulation of a joystick mounted to the rear spherical linkage. The axis of each hinged connection in the spherical linkage converges to a common point in space to form an RCM. The angle between each hinged connection in the spherical linkage defines the size and shape of the operating envelope of the kinematics frame. The base link (**Figure 3.1**, L_1) defines the reference axis of the rotational coordinate system, which is fixed at the RCM. The encoders mounted on the robot base are used to measure the relative angles between: the two successive linkages (**Figure 3.1**, links: L_1 and L_2) and between the links L_1 and base respectively.

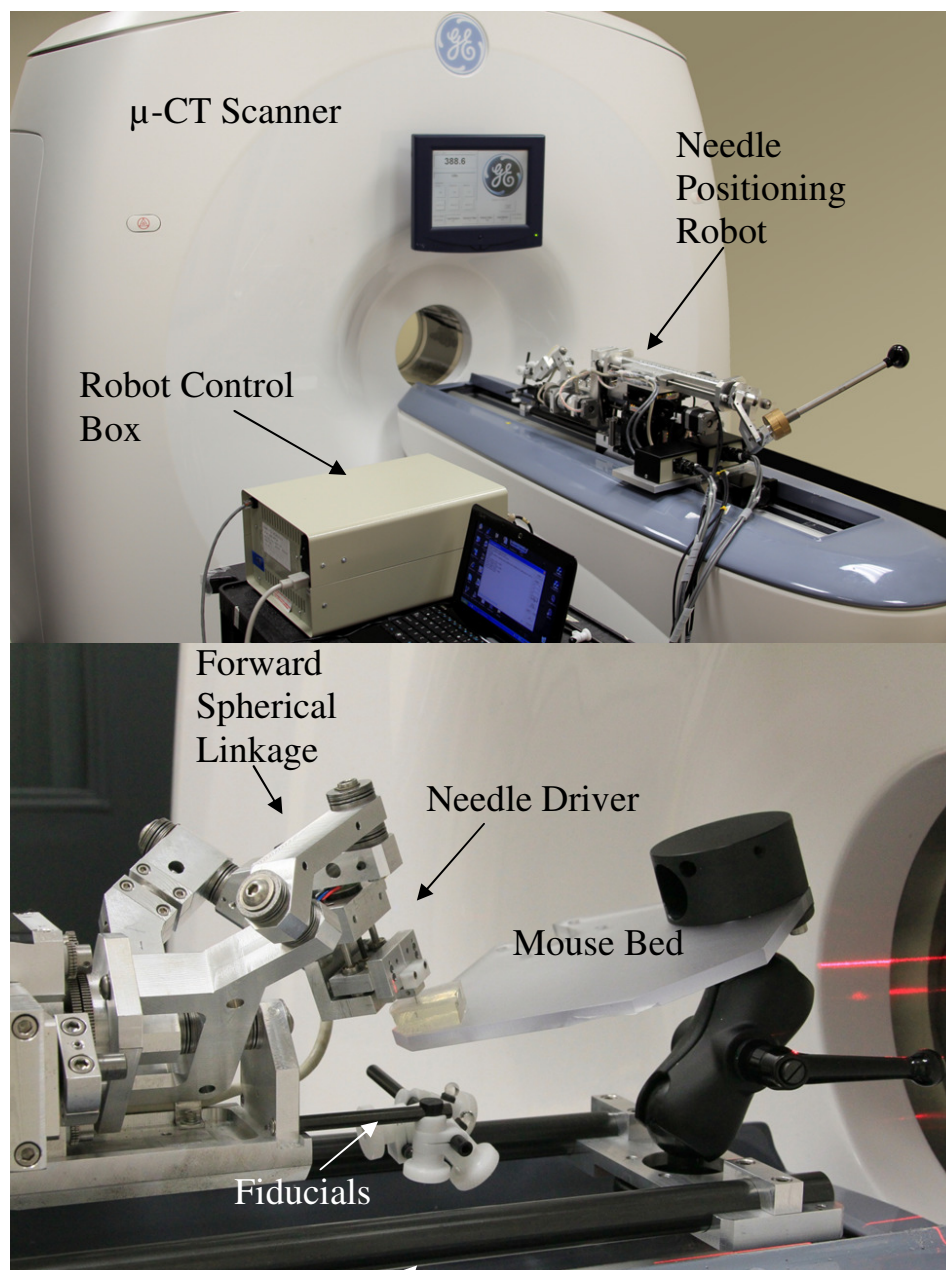


Figure 3.2- **(Top):** Photograph of the robotic apparatus mounted on the CT scanner animal couch and control system. The mechatronic apparatus consists of an XYZ linear stage which supports the spherical linkage. **(Bottom)** Photograph of the forward spherical linkage and attached needle driver. The needle driver is mounted such that the axis of the needle intersects the RCM of the spherical linkage. The mouse bed is attached to a double ball joint which in turn is clamped to the animal couch via a pair of hollow aluminum rails giving a total of 6 degrees of freedom. The fiducials mounted to the aluminum shaft below the mouse bed are used to register the robot to the CT scanner. This registration will account and correct for the variability introduced when the robot was reattached to the micro-CT.

The forward spherical linkage consists of six links and five hinged connections supporting the needle driver. The rear linkage is a mirror image of the forward linkage and consists of five linkage elements and four hinged connections. The extra pinned connection in the forward assembly is used to adjust the axis of each pinned connection in the base link to create a precise RCM. **Figure 3.1** shows a schematic representation of the RCM linkage design.

To determine the stability of the RCM, a precision tooling ball (6.35mm diameter, part 29011, Jergens Inc., Cleveland, OH) was attached to the linkage and aligned to the RCM. The tooling ball displacement throughout the spherical linkages full range of motion was measured using a calibrated XYZ stage (M-462, Newport Corp., Irvine, CA) and attached indicator (Model 25164-10, The L.S. Starrett Company, Waite Park, MN). The measured tooling ball deviation was $< 12.5 \mu\text{m}$ along the X-, Y- and Z-axis.

The motorized needle driver is mounted to the forward spherical linkage to insert and retract the needle (**Figure 3.2**). The needle driver is mounted such that the axis of the needle intersects the RCM of the spherical linkage. The robot implements the RCM in a unique fashion compared to previous designs for small animal interventions. The RCM of the system is positioned at the target location within the animal using the 3-axis XYZ linear stage. Next, the needle driver inserts the needle to the RCM location, which also corresponds with the target. This is a clear divergence from previous robotic designs where the RCM is typically placed on the skin surface. The RCM is positioned at the target rather than the skin to improve targeting accuracy through simplification of the needle driver design. The needle driver is not required to position the needle tip at a range of depths. Rather, the needle driver only needs to position the needle tip in either an inserted or retracted position. The use of a hard stop to control the needle's inserted position eliminates the need for encoders to track the driver position. As part of the robot calibration procedure, the needle is adjusted to locate the inserted needle tip position at the RCM of the robot's linkages.

The electronics of the robot are divided into two separate control systems: one system for the XYZ stage and one system for the spherical linkage and needle driver.

The spherical linkage and needle driver are driven by stepper motors controlled by a multi-axis dual-loop controller (MAXNet, Pro-Dex Oregon Micro Systems, Oregon, WA) and stepper motor drivers (BSD-01v2, Interinar Electronics, Tampa, FL). The XYZ stage is powered by three stepper motors coupled to lead screws. The stepper motors are controlled by a multi-axis controller with integrated stepper motor drivers (DMC2133 with SDM-20242, Galil Motion Controls, Rocklin, CA). Each axis of the XYZ stage contains a linear encoder, which feeds into the multi-axis controller. Custom closed-loop software on the controller monitors the encoders to compare the target position of each axis against their desired position. Both control systems are interfaced to a host PC via an Ethernet hub. Custom software on the host PC sends programs and commands to each of the controllers. The user enters the desired position and orientation of the needle into the PC. The software then uses appropriate inverse kinematic equations to calculate the appropriate commands to send to each controller.

3.2.2 Robot Calibration

3.2.2.1 Coordinate System Calibration

The coordinate system of the robot was calibrated to ensure accurate control of the robot position. The coordinate system of the robot is aligned to the 3-axes of the XYZ linear stage and tracks the position of the device's RCM. The RCM position was calibrated by repositioning the XYZ linear stage at 7.5 mm increments along each axis: covering a total range of ± 15.0 mm, ± 15.0 mm and ± 7.5 mm. At each position, the encoder count for each of the XYZ linear stage's three axes was recorded using a depth gauge (Model 2776S, Mitutoyo Canada, Toronto, ON) mounted onto a calibrated manual XYZ stage (M-462, Newport Corp., Irvine, CA). The encoder step size for the XYZ linear stage was calculated by averaging the measurements along each axis. The flatness, straightness and perpendicularity of each axis of the XYZ linear stage were also verified using a granite surface plate (Grade B-18, The L.S. Starrett Company, Waite Park, MN), indicator (Model 25164-10, The L.S. Starrett Company, Waite Park, MN) and the same calibrated manual XYZ stage used earlier to determine the stability of the RCM. Flatness was evaluated by running the indicator along the surface of the stage for each of the three translational axes and recording any deviations. Straightness was evaluated by placing

the indicator onto a surface perpendicular to a translational axis. The stage was then advanced a known distance along the axis and this distance compared to the distance measured by the indicator. The straightness measurement was completed three times; once for each of the translational axes. The perpendicularity was evaluated by placing the indicator against surfaces parallel to a translational axis. The stage was then advanced along the axis and the indicator recorded for any motion. The deviation of the flatness, straightness and perpendicularity was: $\leq 1.81 \mu\text{m}$, $\leq 0.77 \mu\text{m}$ and $\leq 74.4 \mu\text{rad}$ respectively. These values were all measured over 20 mm of stroke.

The angular orientation of each of the two arms in the forward spherical linkages was also calibrated. The robotic system was first placed onto a granite surface plate, which served as a reference plane. Each of the two arms was independently orientated so that one arm was in a plane perpendicular and one arm was in a plane parallel to the granite surface. Each arm was adjusted to within $2.5 \mu\text{m}$ of the perpendicular or parallel plane using the same calibrated manual XYZ stage and indicator as earlier. The encoder values of the two encoders in the spherical linkage were recorded with the arms in this orientation. The two arms were then rotated 90 degrees once. The encoder values of the second orientation were recorded giving the step size and absolute reference of the encoder home position.

3.2.2.2 Optical-Based Needle Calibration to RCM

To complete an intervention the RCM of the robot is translated to correspond with the localized position of the target. It is therefore of the utmost importance that the needle tip reaches the RCM when it is at the inserted position. Thus, a method to accurately calibrate the needle tip to the RCM is critical to the success of the robotic system. Waspe *et al.* previously developed a method to evaluate the RCM calibration of a needle in a robotic system for small animal interventions [17]. The method involved photographing the needle tip using a high-resolution macro lens. The camera was fixed in two planes perpendicular to each of the robots rotational axes. In each plane a 23G needle was photographed at predetermined angles throughout the respective axes full range of motion. In each photograph the needle was then segmented and its center line calculated. Using the center lines, the location of the RCM was calculated by

determining the center of rotation of the needle axes. The calibration error was determined by calculating the distance of the needle axes from the RCM point. Unfortunately, this calibration method is limited given our robotic system RCM implementation. The method by Waspe *et al.* only accounts for the location of the needle axis and not the needle tip. The needle axis may travel very closely to the RCM; but, the needle tip may be much further from the RCM depending upon its insertion depth. Thus, the needle may miss the target even through the reported calibration error was quite small. To avoid this problem, the calibration method of Waspe *et al.* was modified to account for the needle tip position.

Calibration of the robot was again completed using a CCD camera (EOS-1D Mark IV, Canon Canada Inc., Mississauga, ON) and a high-resolution macro lens (MP-E 65 mm f/2.8 1-5x, Canon Canada Inc., Mississauga, ON). The pixel size of the images captured using this camera and lens was approximated to be 1.0 μm . A length of 27 gauge drill stock (Model 3009A239, McMaster-Carr, Aurora, OH) sharpened to form a conical tip was mounted onto the needle driver. The insertion depth of the needle was adjusted using a set-screw on the needle driver. The set-screw was iteratively adjusted until the magnitude of tip motion in both rotational axes was minimized in the camera viewfinder. The needle was then photographed in two planes perpendicular to each of the rotational axes. For each plane the needle was photograph five times at approximately equally spaced angular positions. In the pitch axis the needle was photographed over a range of: 60 degrees. In the roll axis the needle was photographed over a range of: 120 degrees.

Once all the photographs had been acquired, the needle tip was segmented in each image using a semi-automated algorithm developed in MATLAB (The Mathworks Inc., Natick, MA). A Sobel edge detector was first applied to the needle tip images. The identified edge points from the Sobel edge detector, which followed the outer edge of the needle tip were detected based on a user initialization. A linear least squares regression was applied to the detected points to determine the lines of best fit for each of the two edges of the needle tip. The bisector of the two lines of best fit was then calculated. The needle tip location was finally determined by calculating the intersection of the bisector

with the detected points of the needle edge. This process was repeated for each photograph to yield a set of tip positions for each of the planes. The calibration error in each plane was then calculated by determining the total range of movement of the needle tip over the full range of motion in the two rotational axes.

3.2.2.3 Fixture-Based Needle Calibration to RCM

A calibration fixture was introduced to simplify the needle tip calibration process. The fixture consists of a Delrin plastic block with a flatness verified to within $25.4\text{ }\mu\text{m}$ (**Figure 3.3**). The calibration fixture was itself verified to ensure its top surface matched the RCM position. The fixture was mounted to the robot using two 6.35 aluminum shafts (**Figure 3.3**). The shafts were machined to have an approximate $200\text{ }\mu\text{m}$ eccentricity in its diameter. By rotating the aluminum shaft, the top surface of the calibration fixture can be adjusted upwards and downwards to match the RCM location. The correct height of the block was determined by mounting the fixture to the robot and advancing the needle driver to the fully inserted position. A needle was then placed into the loosened needle holder of the driver. The needle was slowly lowered in the holder until its tip was at the surface of the Delrin block. The needle tip was identified as being at the block surface by lightly sliding a $25.4\text{ }\mu\text{m}$ steel shim back and fourth while lowering the needle. The needle tip caught the shim and no longer allowed it to slide freely when in contact with the needle tip. The needle holder was then tightened to fix the inserted needle tip to correspond with the block surface. The calibration block was then detached from the robot and the needle tip observed using the viewfinder of the camera and macro lens. This process underwent several iterations of adjusting the calibration fixture until needle motion was minimized in the camera viewfinder. With needle motion minimized, the eccentric shaft was fixed with a set-screw to maintain the appropriate calibration fixture position. The calibration fixture can then be mounted to the robot and used to calibrate the needle tip as needed.

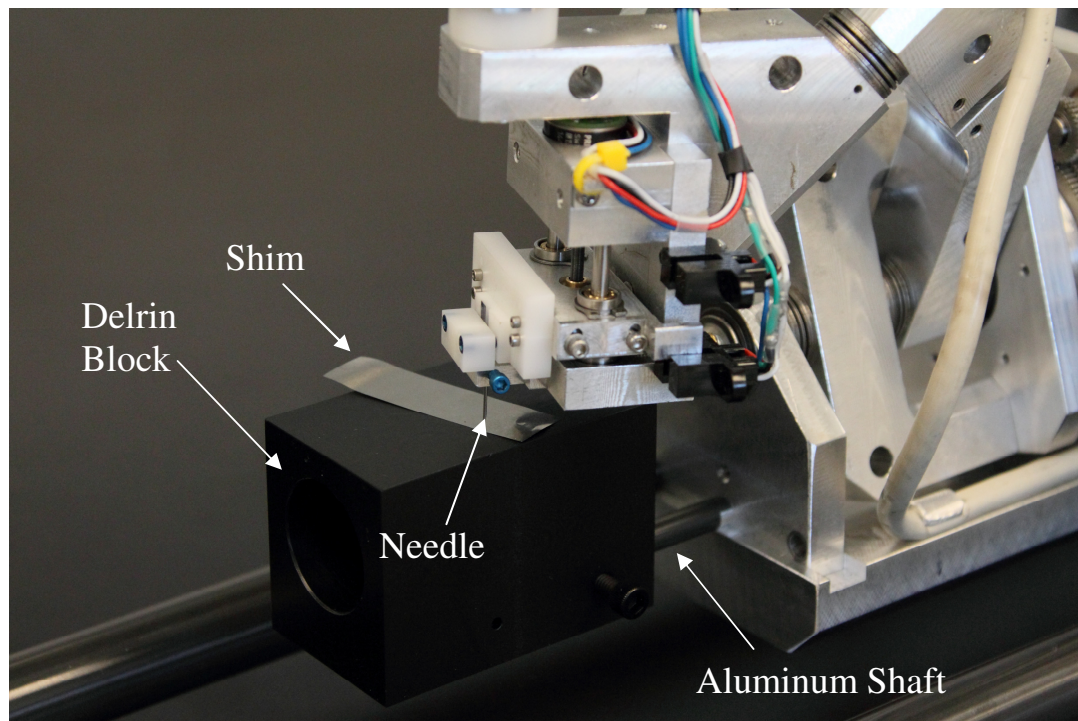


Figure 3.3- Photograph of the calibration fixture used to set the needle tip position at the RCM when the needle driver is in its forward position. The fixture consists of a Delrin plastic block which is mounted to the robot via two aluminum shafts, one attached to the block and one attached to the robot (same shaft supporting the fiducials visible in **Figure 3.2**). The needle height was set by slowly lowering the loosened needle its tip was at the surface of the shim on top of the Delrin block.

The calibration fixture possesses the advantage of reducing the time required to complete needle calibration. Optical calibration of the needle with a camera requires an iterative process of adjusting the needle insertion depth every time the needle is calibrated. Iterative calibration is time consuming and requires approximately 30 minutes to complete. On the other hand, use of the calibration fixture requires only one iterative calibration of the fixture itself. Once the fixture itself is calibrated, it can be mounted to the robot and used to calibrate the needle tip in less than five minutes. The results of the calibration using the fixture were validated using the camera and macro lens. The needle was again imaged at 5 approximately equally spaced positions in planes perpendicular to the roll and pitch axes. The needle tips were then localized in each of the photographs using the previously described technique. The calibration error was calculated by determining the total range of movement of the needle tip in each plane. The calibration

results of the calibration fixture where compared to the iterative optical calibration results to determine the difference in the accuracy of the two methods.

3.2.2.4 Needle Tip Repeatability

The repeatability of the needle driver was characterized to ensure the stability of the needle tip calibration. The needle tip will quickly become un-calibrated if the needle driver does not consistently and reproducibly place the needle tip to the correct depth, which corresponds with the RCM. To characterize the needle driver repeatability, the needle orientation was adjusted to be fully upright using the spherical linkage encoders. The needle was then inserted and retracted a total of nine times while maintaining a constant needle orientation. Each time the needle was inserted, it was photographed using the high-resolution macro lens. The location of the tip was calculated in each of the nine photographs using the needle tip localization technique described during RCM calibration. The repeatability was characterized by determining the standard deviation of the needle tip position in the photographs.

3.2.3 Robot to micro-CT Registration

3.2.3.1 Registration Process

A two-stage registration process was developed to register the coordinate system of the robot to the micro-CT scanner (eXplore Ultra Locus, General Electric Healthcare Biosciences London, ON, Canada). The two-stage registration was developed to achieve a balance between attaining a high quality registration with the time requirements of the end user to complete a pre-clinical intervention. Completion of the primary first step of the registration requires that a removable 6.35 mm borosilicate fiducial bead be mounted onto the device at the RCM (McMaster-Carr, Cleveland, OH). In addition, an array of 6 more borosilicate bead secondary fiducials was mounted onto the robot below the animal bed (fiducial array visible in **Figure 3.2**). With the RCM fiducial bead attached, the robot was positioned at four different locations within the micro-CT bore and a CT image was obtained each time. Using registration software developed in MATLAB (The Mathworks Inc., Natick, MA), the rigid body transformation between the two sets of coordinates was calculated by comparing the position of the RCM fiducial in robot

coordinates to its position in each of the four images. This primary registration can be used alone to guide to the robot to targets in micro-CT images. However, if the robotic system is removed and then reattached to the micro-CT bed, this primary registration is no longer valid due to variability in robot reattachment [16]. Unfortunately, repeating the primary registration each time the robot is reattached to the micro-CT to complete an intervention would be time consuming and laborious. To avoid constant repetition of the primary registration a secondary registration was developed.

The secondary registration takes advantage of the 6 borosilicate secondary fiducials attached to the robot below the animal bed (**Figure 3.2**). During primary registration, these six secondary fiducials are imaged along with the RCM fiducial bead. One of the scans acquired for the primary registration is of the robot at its home position. To complete the secondary registration, the reattached robot and six secondary fiducials are imaged with the robot at its home position. The registration software is then used to calculate the rigid body transformation using the six secondary fiducial positions in the primary registration home scan and the secondary fiducial positions in the secondary registration home scan. This secondary registration will account for and correct the variability introduced when the robot is reattached to the micro-CT scanner. A target in the micro-CT images can then be localized in robot coordinates by applying both registrations. Through the secondary registration, the end user is only required to acquire one image at the initiation of an intervention rather than four. Furthermore, imaging of the fiducials for secondary registration can be simultaneously acquired while imaging the small animal to localize targets. Since the small animal must always be imaged, the secondary registration does not increase the total number of scans required and allows for the primary registration to be reused across multiple interventions. Unfortunately, use of the secondary registration will also reduce overall targeting accuracy since two registration errors, from the primary and secondary, will be combined. The primary registration can be used by itself to improve targeting accuracy; however, this will be at the expense of increasing total registration time. Use of the combined registration reduces time for procedures at the expense of accuracy. The end-user must determine which registration process will best suit their application needs.

3.2.3.2 Registration Software

The fiducial bead mounted onto the robot RCM was segmented and its centroid was determined in each of the four images acquired for the primary registration. Segmentation was accomplished through a threshold based region-growing. The center of the segmented RCM fiducial was then calculated using a squared-intensity-weighted centroiding. The centroiding algorithm used was found in simulated images to have an error of $< 5\%$ of the image voxel size in localizing 3D centroids [23]. The RCM fiducial centroid positions were then rigidly registered to their homologous robot coordinates using a least squares algorithm [24]. The results of the primary registration represented the translation and rotation required to align the coordinate system of the micro-CT scanner with the robotic system.

The secondary registration first required that on the day of the primary registration, with the robot at its home position, the centroids of the six secondary fiducial beads be determined using the technique previously described. On the day of the secondary registration, again with the robot at its home position, these six secondary fiducials are reimaged and their centroids determined. The two sets of centroids are then registered using a rigid body transformation. This secondary registration represents the transformation required to realign the robot axes on the day of the intervention with the robot axes on the day of the primary registration. The errors of the primary, secondary and combined registration were characterized by calculation of the fiducial registration error (FRE) and target registration error (TRE) [25]. The TRE of the primary registration was calculated by acquiring five additional images, not used in the registration, of the RCM fiducial at positions in the robots full range of motion. The secondary and combined TREs was calculated by attaching and reattaching the robot to the micro-CT scanner bed five times with the RCM fiducial still attached. In each image, five of the six secondary fiducials were used to calculate the secondary registration. The sixth secondary fiducial in each of the five images was used to calculate the secondary TRE. The combined TRE in these five images was calculated using the position of the RCM fiducial in the images following robot reattachment to the scanner bed.

3.2.4 Robot Targeting Accuracy

3.2.4.1 Targeting Accuracy Phantom Design

Tissue-mimicking phantoms were used to quantify the targeting accuracy of the robotic device. The phantoms consist of a 15% by weight gelatin solution (Porcine Skin Type A, Sigma-Aldrich, St. Louis, MO) which forms a cross-linked matrix [26].

3.2.4.2 Targeting Accuracy Experiment

Two separate sets of targeting experiments were completed. The first set used the combined registration process to guide the robot to targets in tissue-mimicking phantoms. The second set used only the primary registration to guide the robot. For each set, the targeting phantoms was first secured to the phantom holder of the robotic device and the robot inserted into the bore of the eXplore Locus Ultra micro-CT scanner. The phantom was then imaged using a 16 second anatomical scan at 140 kVp and 20 mAs. The image was reconstructed to yield an image with 153.9 μm isotropic voxel size (example shown in **Figure 3.4**). The image of the phantom was then visualized within MATLAB. Ten image voxel coordinates within the phantom were manually localized and selected as target positions. For each set, the location of each of the 10 target voxel coordinates within robot coordinates was calculated using either a combined registration or a primary only registration. For each target, the robot RCM was placed at the target location, the needle inserted and an image acquired. Throughout the targeting experiments the needle angulation remained constant at approximately 90 degrees in the roll axis and 45 degrees in the pitch. Needle angulation was maintained constant to allow targeting accuracy to be quantified independently of angle.

For each acquired image, the distance of the needle from target voxel coordinates was determined by first segmenting the inserted needle using a threshold-based region growing algorithm. The center line of the needle in the image was estimated using principal components analysis (PCA) to fit a 3D line to the segmented needle. The targeting accuracy was quantified by calculating the distance of each 3D fitted line to the target voxel. The distance of the line to the target voxel represents the accumulation of

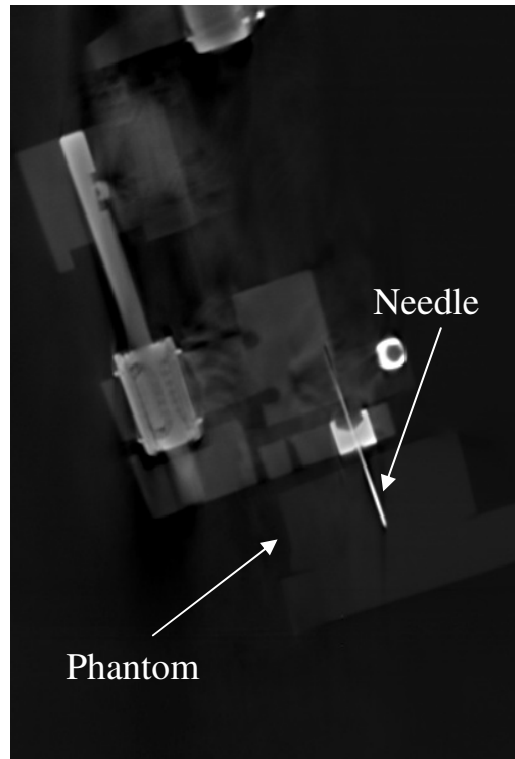


Figure 3.4- View of reconstructed CT image used for the needle targeting experiment. For each target, the robot RCM was placed at the target location, the needle inserted and an image acquired. For each acquired image, the distance of the needle from target voxel coordinates was determined by first segmenting the inserted needle using a threshold-based region growing algorithm. The center line of the needle in the image was estimated using principal components analysis (PCA) to fit a 3D line to the segmented needle.

error from a number of sources including: robot positioning error, registration error, needle calibration error and needle deflection.

3.2.4.3 Needle Angulation Accuracy

We used a gelatin phantom to evaluate the variation in needle positioning over the full range of needle angulation. The gelatin phantom was placed onto the animal bed of the robot and the robot was then oriented in seven different positions (see **Table 3.2**) covering the angular range of the robot motion. At each orientation the needle was inserted into the gelatin phantom and imaged by the micro-CT scanner. In each image, the needle center-line was calculated using the same technique previously described. Ideally, all seven center-lines should intersect at a common point in space (*i.e.*, the RCM) if no variation in needle positioning is present with angulation. An iterative solution was used to calculate the point in space with the smallest sum of squares distance from each

of the centerlines. The variation in needle positioning over the full range of needle angulation was then quantified by calculating the distance of each center-line to the point of best fit.

3.2.5 Preclinical Application

All *in vivo* imaging was performed under a protocol approved by the University Health Network Animal Care and Use Committee. Measurements were performed in two female SCID mice, each bearing a single subcutaneous human cervix carcinoma tumour (ME180). A tumour was established in the first mouse by suturing a 2–3 mm³ tumor fragment along with a 1.5 mm radio-opaque pellet (Beekley Co., Bristol, CT) into the dorsal subcutaneous tissue. A tumour was established in the second mouse by suturing a 2–3 mm³ tumor fragment into the subcutaneous tissue of the hind limb. The experiment was performed once the tumours reached approximately 1 cm in diameter. The mice were anesthetized using a 2% by volume isoflurane-oxygen mixture, the hair removed from their tumours' areas, and immobilized in a supine position with their front and back paws taped to a custom built mouse platform mounted on the robot. The mice were imaged using a standard anatomical imaging protocol consisting of a 16 second scan with an 80 kVp and 60 mAs. The images were reconstructed to yield a 153.9 μ m isotropic voxel size.

The mouse bearing the dorsal tumour with the implanted radio-opaque pellet was used to evaluate the robot's ability to perform image guided needle placement *in vivo*. Similar to *in vitro* experiments, a 23G needle was mounted on the needle driver. The tumour was immobilized by taping it onto a plastic block and surrounding it with pieces of rigid foam. A pre-needle insertion CT scan was performed to visualize the radio-opaque pellet. The robot RCM was placed at the centre of mass (CM) of the radio-opaque pellet and the needle was inserted. A post-needle insertion scan was acquired to confirm successful contact with the target. This process was repeated for 3 angles of insertion chosen randomly and the distance between the needle tip and surface of the radio-opaque pellet measured.

IFP measurements were performed in the mouse bearing the hind limb subcutaneous tumour using the wick-in-needle technique [27]. Measurements were made using a 23G needle containing both a front and side port connected to a pressure transducer (Model P23XL, Harvard Apparatus, Canada), which in turn was connected to a data acquisition system (PowerLab 4/35 with LabChart Pro, ADInstruments Pty Ltd., USA) through 50 cm of PE20 polyethylene tubing (Becton Dickinson, Franklin Lakes, NJ, USA). The entire system was flushed with a heparin sulphate/saline solution (1:10). A pre needle insertion scan was performed, the tumour indentified, and a position chosen such that the side port of the needle would be inside the tumour volume, while the front port would be in healthy tissue. IFP measurements were made as the needle was inserted and maintained for 30 sec after reaching the target location. A post-needle injection scan was performed to confirm the location of the needle inside the tumour. The needle was then retracted by approximately 3 mm while continuously monitoring IFP. These two positions were chosen to demonstrate the importance of correctly needle placement on stable IFP measurements.

3.3 Results

Table 3.1 provides a summary of the results obtained for each of the experiments described in the methods.

3.3.1 Robot Calibration

3.3.1.1 Error in Optical-Based Needle Calibration to RCM

The RCM calibration error represents the range of motion of the needle tip as the robots rotational axes are moved through its full range of motion. In the roll plane, the RCM calibration error range was found to be $\Delta_x = 43 \mu\text{m}$ and $\Delta_y = 28 \mu\text{m}$, where the x- and y-axis represent the horizontal and vertical axis orientated perpendicular to the z-axis which represents the long axis of the CT bore. In the pitch direction the RCM calibration error was $\Delta_y = 69 \mu\text{m}$ and $\Delta_z = 30 \mu\text{m}$. Added in quadrature the total errors were $\text{Error}_{\text{Roll}} = 51 \mu\text{m}$ and $\text{Error}_{\text{Pitch}} = 75 \mu\text{m}$. The maximum calibration error is expected to occur at the extremes of the rotational axes. **Figure 3.5** displays a composite photo of the calibration photos and the segmented needle tip locations.

Table 3.1-Summary of the results obtained for each experiment.

		<i>Error (μm)</i>
3.2.2.2 Error in Optical-Based Needle Calibration		
Error to RCM		
<i>Roll plane</i>		
Δ_x		43
Δ_y		28
<i>Pitch plane</i>		
Δ_y		69
Δ_z		30
3.2.2.3 Error in Fixture-Based Needle Calibration		
Error to RCM		
<i>Roll plane</i>		
Δ_x		36
Δ_y		70
<i>Pitch plane</i>		
Δ_y		11
Δ_z		5
3.3.1.3 Needle Driver Repeatability		
σ_{needle}		± 9
3.3.1.4 Robot Registration		
<i>Primary</i>		
$\text{FRE}_{\text{primary}}$		21 ± 6
$\text{TRE}_{\text{primary}}$		31 ± 21
<i>Secondary</i>		
$\text{FRE}_{\text{secondary}}$		70 ± 25
$\text{TRE}_{\text{secondary}}$		79 ± 14
<i>Combined</i>		
$\text{TRE}_{\text{combined}}$		139 ± 63
3.3.2 Robot Positioning Accuracy		
<i>Primary Registration Positioning Accuracy</i>		
$\text{Total}_{\text{error}}$		131 ± 25
<i>Combined Registration Positioning Accuracy</i>		
$\text{Total}_{\text{error}}$		206 ± 20
3.3.2.3 Needle Angulation Accuracy		
$\sigma_{\text{angle}} (< 50^\circ)$		72 ± 62
$\sigma_{\text{angle}} (< 30^\circ)$		51 ± 31

3.3.1.2 Error in Fixture Based Needle Calibration to RCM

RCM calibration was also completed using a precision calibration block. In the roll plane, the RCM calibration error was $\Delta_x = 36 \mu\text{m}$ $\Delta_y = 70 \mu\text{m}$. In the pitch plane the RCM calibration error was $\Delta_y = 11 \mu\text{m}$ and $\Delta_z = 5 \mu\text{m}$. Added in quadrature the total errors were $\text{Error}_{\text{Roll}} = 75 \mu\text{m}$ and $\text{Error}_{\text{Pitch}} = 12 \mu\text{m}$.

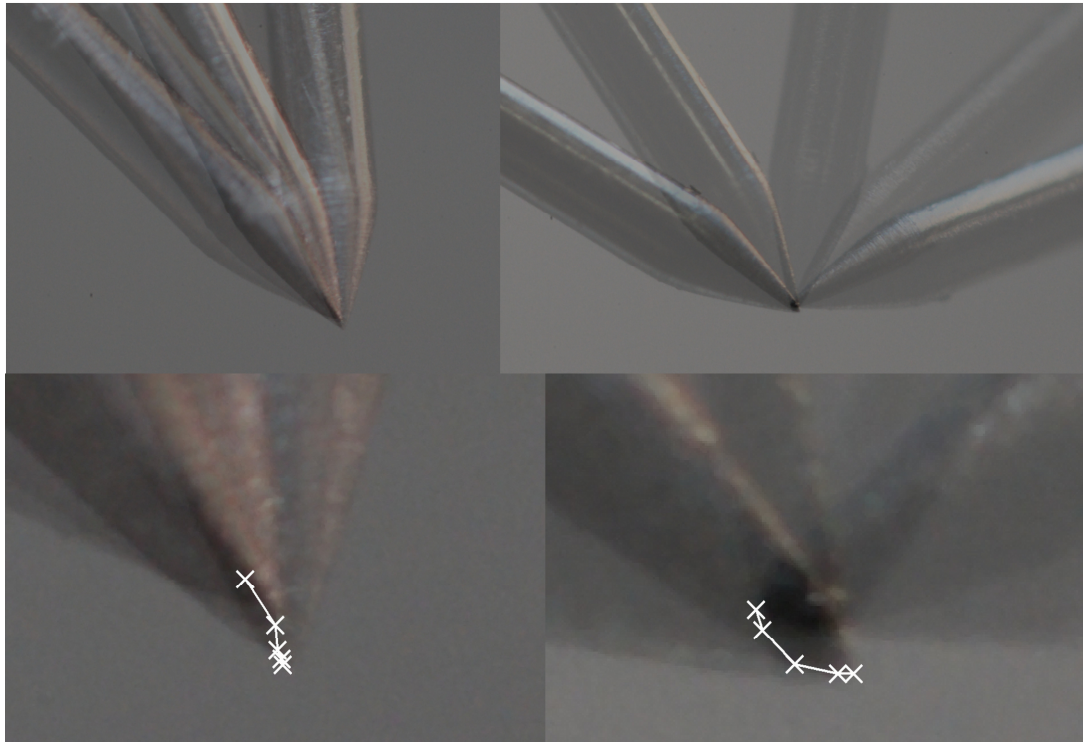


Figure 3.5- Composite photographs of the calibration photos showing the pitch (**Top Left**) and roll (**Top Right**) of the needle throughout its full range of motion. The bottom two photographs shows a close-up view of the segmented needle tip locations in the- pitch (**Bottom Left**) and roll (**Bottom Right**) directions.

3.3.1.3 Needle Driver Repeatability

The needle driver must consistently position the needle tip at the same location in space following repeated insertions and retractions. Significant variations in needle positioning by the needle driver will reduce the ability of the system to maintain calibration. The needle driver repeatability is the standard deviation of needle depth in multiple insertion procedures. The needle driver repeatability was found to be $\sigma_{\text{needle}} = \pm 9 \mu\text{m}$.

3.3.1.4 Robot to micro-CT Registration

The primary robot registration is the transformation required to convert the micro-CT scanner coordinate system to the robot coordinate system, and was calculated using the location of the fiducial bead at the RCM of the robot. The fiducial localization and registration errors were found to be $\text{FRE}_{\text{primary}} = 21 \pm 6 \mu\text{m}$ and $\text{TRE}_{\text{primary}} = 31 \pm 12 \mu\text{m}$.

The secondary robot registration is the transformation required to relate the robot coordinate system on the day of an intervention to the day of the primary registration, and was calculated using fiducials fixed to the robot frame. The fiducial localization and registration errors were found to be $FRE_{\text{secondary}} = 70 \pm 25 \mu\text{m}$ and $TRE_{\text{secondary}} = 79 \pm 14 \mu\text{m}$.

The combined registration is the combined transformations performed in the primary and secondary registrations. The combined registration error represents the total error of the complete registration process. Since the combined registration itself has no fiducials, there is no fiducial registration error to report. For the combined registration the $TRE_{\text{combined}} = 139 \pm 63 \mu\text{m}$.

3.3.2 Robot Positioning Accuracy

3.3.2.1 Combined Registration Positioning Accuracy

The needle positioning accuracy is the distance of the segmented needle track in the gelatin phantom from the target pixel in a micro-CT image. The targeting experiments were completed with the rotational axes of the robot approximately constant: with the needle pose at 90 degrees in the roll plane and 45 degrees to the CT bore as seen in the pitch plane. The calculated mean targeting errors along the three images axes were: $X_{\text{error}} = 194 \pm 16 \mu\text{m}$, $Y_{\text{error}} = 33 \pm 17 \mu\text{m}$ and $Z_{\text{error}} = 57 \pm 19 \mu\text{m}$. The total mean error of the needle position was $Total_{\text{error}} = 206 \pm 20 \mu\text{m}$. An ANOVA test ($p = 0.05$) found a significant difference between the mean targeting errors of each axis. A Tukey test ($p = 0.05$) found the errors of all axes to be significantly different from each other.

3.3.2.2 Primary Registration Positioning Accuracy

A second set of targeting experiments were completed using only the primary registration. The calculated mean targeting errors along the three images axes were: $X_{\text{error}} = 119 \pm 22 \mu\text{m}$, $Y_{\text{error}} = 19 \pm 10 \mu\text{m}$ and $Z_{\text{error}} = 46 \pm 24 \mu\text{m}$. The total mean error of the needle position was $Total_{\text{error}} = 131 \pm 25 \mu\text{m}$. An ANOVA test ($p = 0.05$) found a significant difference in the mean targeting errors of each axis. A Tukey test ($p = 0.05$) found the errors of all axes to be significantly different from each other.

Table 3.2-Summary of needle angulations used to test needle deflection at different angles of attack. The variables α and β represent the angle of the primary and secondary crank measured by the encoders. The angle of attack represents the angle between the needle axis and the normal vector to the surface of the phantom.

Scan	α°	β°	Angle of attack (degrees)	Error (μm)
1	45	135	11	34
2	25	155	14	51
3	25	115	21	24
4	66	155	21	110
5	-5	114	30	34
6	60	178	25	56
7	105	172	50	189

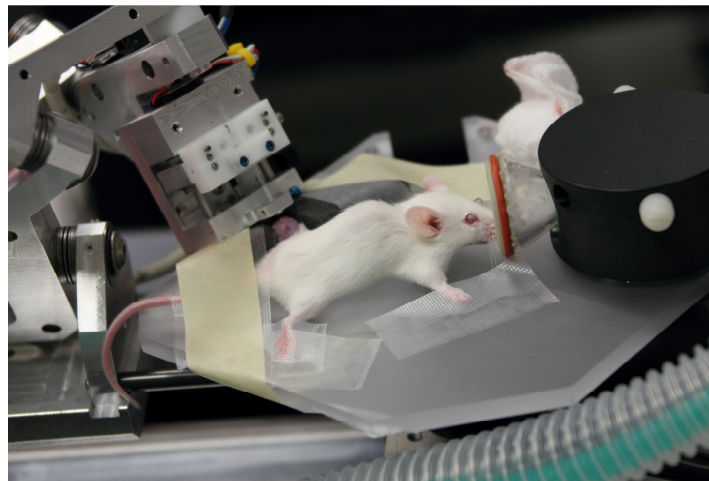
3.3.2.3 Needle Angulation Accuracy

The consistency of needle accuracy was evaluated by inserting the needle multiple times to the same position in space at varying angles of attack (10 - 50 degrees). The results for these experiments are given in **Table 3.2** showing that the average normal distance from each axis to the fixed target was determined to be: $\text{Error}_{\text{angle}} = 72 \pm 62 \mu\text{m}$.

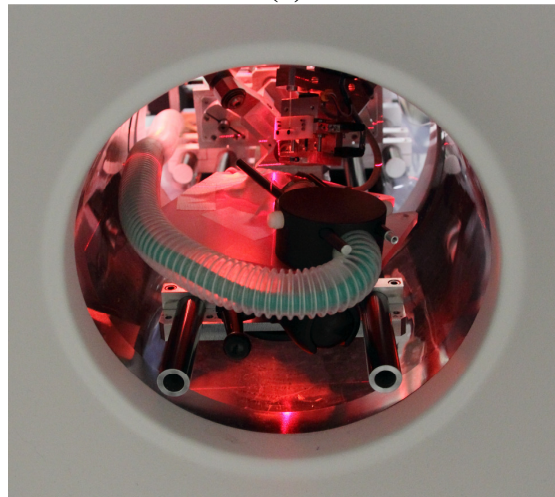
3.3.3 Preclinical Application

The experimental setup used in each of the small animal experiments is shown in **Figure 3.6**. Robot guided IFP measurements were made at two locations in the subcutaneous hind limb tumour. In the first location the post-needle insertion CT scan demonstrated that the front port of the needle was straddling the boundary between tumour and healthy tissue, and the side port was located in the centre of the tumour (**Figure 3.7a**). The needle was then retracted 3 mm and a CT scan showed that both the front and side ports of the needle were inside the tumour volume (**Figure 3.7b**). The accuracy and stability of the wick-in-needle technique requires that both ports of the needle are exposed to a similar external pressure. If the pressure at one port is substantially lower than the other, fluid flow is directed out of the IFP system and a decreasing pressure is measured. Region III of **Figure 3.7c** demonstrates this effect. When the needle was retracted to the second position shown in **Figure 3.7b**, the IFP measurement stabilized (**Figure 3.7b**, region IV). This highlights the importance of using an accurate position system under image guidance to perform reliable IFP measurements.

The robot was used to target a radio-opaque pellet implanted in a subcutaneous dorsal tumour under image guidance. Post needle insertion CT projection images showed that the needle was successfully delivered to the target (**Figure 3.8**). Measurement of the distance between the needle tip and the surface of the pellet was difficult due to partial volume effects and beam hardening artifacts caused by the radio-opaque pellet and steel needle. The measured distance between the needle tip and pellet surface was 0.41 ± 0.12 mm. The CM of the radio-opaque pellet shifted 0.85 ± 0.28 mm relative to its pre-needle insertion position. A real time cine-CT scan of the last needle placement showed that the shift in pellet position was due to contact with the needle as well as tissue deformation during needle insertion.

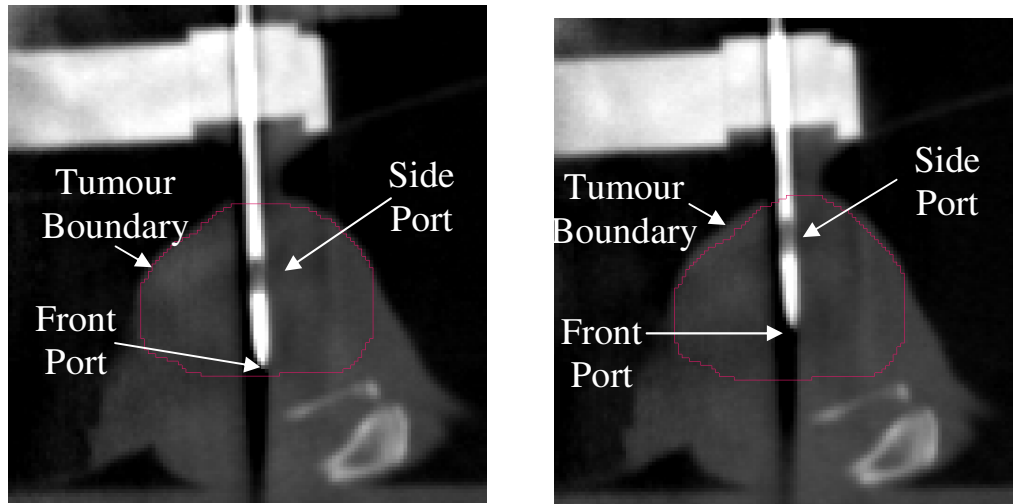


(a)



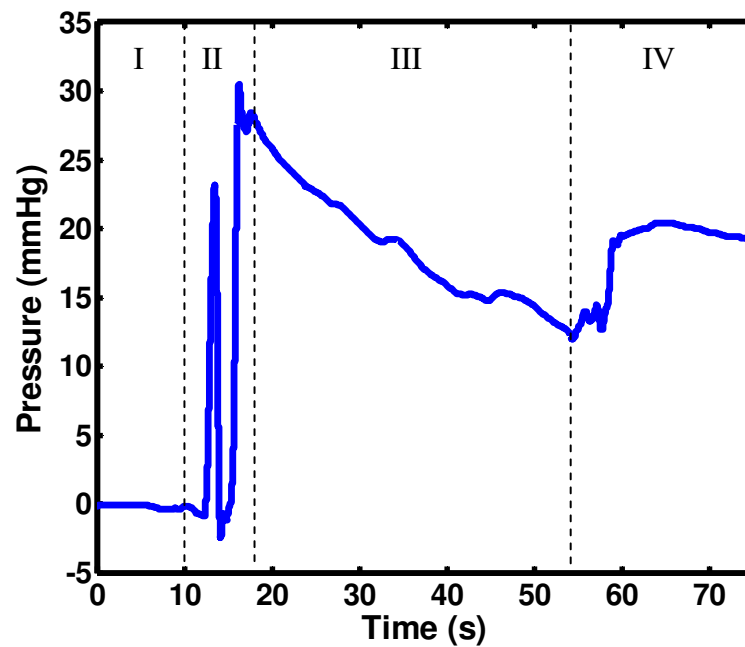
(b)

Figure 3.6- Photograph of the experimental setup used for the animal interventions (**(a)** outside, and **(b)** inside of the bore of the CT scanner. The only part of the apparatus that resides inside of the scanner is the mouse bed and part of the needle driver to minimize artifacts in the image.



(a)

(b)



(c)

Figure 3.7- Wick-in-needle measurements of IFP demonstrating the importance of needle placement for stable and accurate results. (a) shows the front port of the IFP needle straddling the tumour boundary (outline), while the side port is in the centre. (b) both the front and side ports are within the tumour boundary (outline). (c) Results of IFP measurements showing: (I) the pre needle insertion baseline; (II) the signal as the needle is inserted; (III) the measured IFP at the position shown in (a); and (IV) the measured IFP at the position shown in (b).

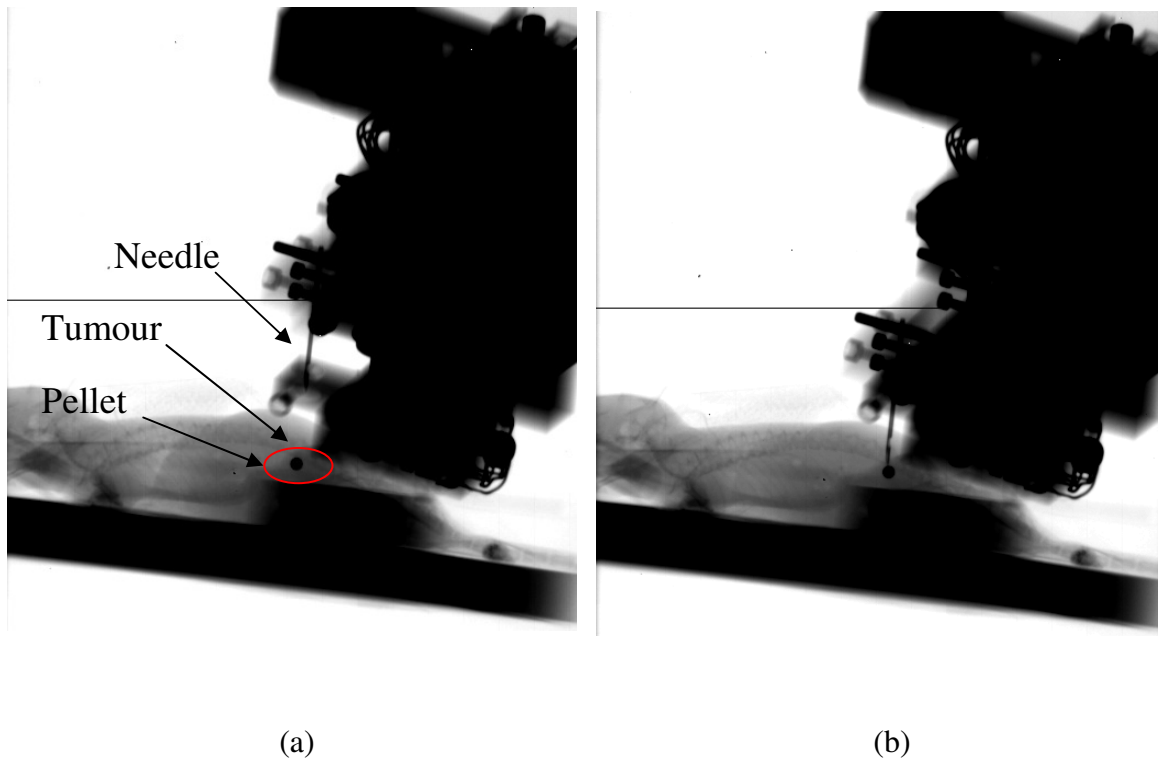


Figure 3.8- Projection views obtained from two sequential CT scans which demonstrate the ability to perform image-guided needle placement *in vivo*. (a) A pre needle insertion image highlighting the location of the needle, the tumour (red outline), and the radio-opaque pellet (fiducial). (b) A post needle insertion image showing the needle making contact with the radio-opaque pellet.

3.4 Discussion

3.4.1 Robot Calibration

During the initial setup of the robot linkages, the RCM of the robot was found to remain relatively fixed in space with a maximum deviation of $12.5\ \mu\text{m}$. As a result, the calibrated needle tip would be expected to track a path corresponding closely to the surface of a sphere when the robot is adjusted through its full range of motion. The center of the sphere is the RCM position and the radius of the sphere is the needle calibration error. The calibration error is quantified by measuring the range of pixels the needle travels along each axis in each plane. As shown in **Figure 3.5**, the Δ_x and Δ_z errors should be equal and the two Δ_y errors should both be equal to half this value. Furthermore, the segmented needle tips in both planes should form a circular path. However, this is not true for the obtained results. A number of sources of error exist in the methods used

to cause the measured calibration error to deviate from this ideal case. First, the use of photography to validate the calibration results in a 3-dimensional path being projected onto a 2-dimensional plane. Errors in positioning the camera truly perpendicular to each of the rotational axes will result in the needle paths failing to track a circular path. Secondly, to measure the radius of the sphere, the needle tip must track a path of at least 90 degrees or greater. In the roll axis, the needle traveled approximately 120 degrees allowing the sphere to be correctly characterized. In the pitch direction the robots range of motion is limited to approximately 60 degrees. The track measured in the pitch axis travels a smaller sector of the sphere compared to the roll axis. The errors measured in the pitch axis will inherently underestimate the calibration error. The roll axis results therefore are a better characterization of the needle calibration errors.

The calibration results demonstrated that the roll axis has the largest error as expected. However, for the optical calibration, the pitch axis contains the largest errors even though the pitch error should be inherently less. The likely cause of this aberration is deflection in the shaft of needle itself. Deflections inherent to any needle will result in overestimates of calibration error as the distance traveled by the needle will be amplified by deflection. Depending on how the needle is mounted, this error may occur in the roll plane, the pitch plane or some combination of the two. Two different needles were used for the optical calibration and the fixture calibration. The needle selected for the optical calibration likely deflected in the pitch direction resulting in an unexpectedly large pitch calibration error. Needle deflection along with the previously discussed sources of error cause the calibration results to deviate from their expected results.

The radius of the calibration error sphere, or the true calibration error, is shrouded behind a number of other unavoidable error sources. However, an estimate of the independent needle tip calibration error can be distilled from reported results. As discussed, the pitch axis lacks sufficient range of motion to accurately estimate the sphere radius. An estimate must therefore come from the roll results. Two potential cases exist for the roll results: either needle deflection occurred in the roll plane or deflection did not occur in the roll plane. If no deflection errors exist in the roll plane, the Δ_y measured in the roll direction should be approximately half Δ_x . This case is true for the optical calibration

results. The radius of the calibration error sphere is therefore approximately equal to the mean of Δ_y and half of Δ_x or 25 μm . If deflection did occur, the relationship between Δ_x and Δ_y no longer holds true. For the fixture calibration, deflection is evident with Δ_y much larger than Δ_x . In the deflection case, the most reasonable estimate of the sphere radius is half of Δ_x . Δ_x is the most reasonable estimate since it corresponds with the calibrated needle axis. For the calibration fixture, the radius can be estimate to be approximately 18 μm . The expected standard deviation of both calibration errors is the needle driver repeatability of 9.1 μm .

The two estimates of the calibration errors for the optical method and fixture method are extremely close and less than one standard deviation apart. The results suggest that the calibration obtained using these two methods are equivalent. However, calibration can be completed much faster using the fixture rather than the iterative optical method. Therefore, the calibration fixture should be the preferred method of completing calibration.

3.4.2 Robot Registration

For the primary registration (robot coordinates to fiducial bead centroids in micro-CT images), the robot coordinates are measured with high accuracy using a calibrated XYZ positioning stage with a measurement resolution of 0.1 μm . However, the secondary registration is a registration of fiducial bead centroids from two different micro-CT images. The secondary registration therefore has the centroiding error in both sets of coordinates; whereas, the primary only possesses the error in one coordinate set. The secondary registration would therefore be expected to have twice the fiducial centroiding error of the primary registration. However, the mean TRE of the secondary registration is approximately 2.5x larger than the TRE of the primary registration. This suggests that much of the TRE arises from Fiducial Localization Error (FLE) in the centroiding of fiducials in the micro-CT images. The registration errors would therefore be expected to be reduced if using a scanner with higher resolution.

Either the primary registration alone or the combined registration can be used to guide the robotic device for interventions. Use of the primary registration would be

expected to result in much higher targeting accuracy with greater repeatability than the combined registration. The combined registration contains the accumulation of many more error sources than the primary registration. The combined registration contains errors from both the primary and secondary registrations along with errors resulting from attaching and detaching the robot from the micro-CT scanner bed. As a result, the primary registration offers the advantage of nearly a fifth of the TRE of the combined registration and a much smaller standard deviation. Unfortunately, the primary registration is more time consuming than the combined registration. Four scans are required to complete the primary registration and they must be repeated every time the robotic system is removed from the scanner bed. In contrast, the combined registration can be completed with a single image, which can be acquired simultaneously with imaging of the small animal. Depending on the application, the end user must determine the ideal balance between time requirements and accuracy.

Waspe *et al.* [16] is the only other method developed to register a robotic system with a micro-CT imaging system. The reported FRE and TRE of the registration process were 96 μm and 210 μm respectively. Both the primary and combined registrations offer a reduction in error over this method.

3.4.3 Robot Positioning Accuracy

The 153.9 μm micro-CT voxel size is relatively large in relation to the desired needle targeting accuracy of 200 μm . Therefore, in order to be able to use the micro-CT to meaningfully quantify targeting error, a technique capable of sub-voxel accuracy is required. Unfortunately, the needle tip cannot be localized to sub-voxel accuracy. Rather, to achieve the desired measurement accuracy, the needle must be segmented and a line of best fit calculated to determine the needle axis in the micro-CT image. The metric used to calculate targeting accuracy is the shortest distance of the needle axis to the target. Unfortunately, this metric does not provide any information about the error in needle depth or its associated variability. Furthermore, the reported errors were measured at a constant angle and do not account for variation in targeting accuracy due to needle angulation. The reported targeting errors therefore underestimate the true targeting error. The measured targeting errors can be corrected to better represent the true targeting error

by using the errors measured during needle calibration and needle angulation testing, which do account for these other factors. Since these errors are all independent their means and standard deviations can be added in quadrature to estimate the true targeting error.

The RCM deviation is known to be a maximum of $12.5\ \mu\text{m}$ through the robots full range of motion. In comparison, the mean error from the point of best for the robot angulation testing was $72 \pm 62\ \mu\text{m}$. Therefore, the variation in angular targeting accuracy is largely not the result of mechanical errors. Rather, this error would largely be due to needle tip calibration error and needle deflection in the tissue-mimicking phantom. Error resulting from needle tip calibration error is constant and should remain near constant with respect to needle angulation. The large standard deviation observed in needle angulation accuracy is likely the result of needle deflection. As shown in **Table 3.2**, the error was the smallest for angles of attack less than 30 degrees from the normal. For these small angles the mean error was $51 \pm 31\ \mu\text{m}$. The error tended to increase with larger angles of attack. For the example illustrated in **Figure 3.9**, for the maximum angle

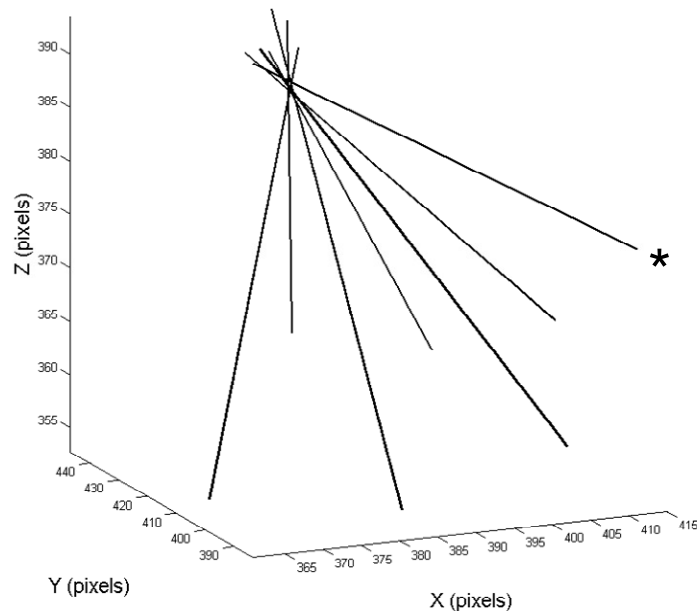


Figure 3.9- A composite image of the needle tracks from the needle angulation accuracy experiment (**Section 3.2.4.3**) All of the needle tracks with exception to one track approached the target point with an angle of attack (from the normal) of less than 30 degrees. The one track labeled as (*) illustrates an exaggerated needle deflection with the needle approaching the target at 70 degrees from the normal, where the needle is perpendicular to the phantom surface.

tested of 50 degrees the error increased to 188 μm . These results are not surprising: the larger the angle of attack, the more obliquely the needle penetrated the phantom surface and the greater the proportion of the needle within the phantom. Both of these conditions are conducive to needle deflection. Targeting error increases with the angle of attack of the robot is largely the result of needle deflection.

A source of error typically neglected in the literature is the rearward deflection of the robot itself during needle insertion. This error is neither accounted for in the robot targeting error or calibration error. The robot deflection is the result of the entire machine shifting due to reactionary forces acting on the needle driver as it advances the needle through the tissue. To determine the magnitude of this deflection in our design, a brass weight, which exerted 10 N of force was mounted to the robot RCM. The deflection of the robot with the brass weight was measured using an indicator to be 151 μm . However, the needle driver is capable of delivering a maximum force of 2 N, which corresponds with a rearward robot deflection of 30 μm . This illustrates the need to make the robot as rigid as possible. Although our system is suitable for inserting needles into soft tissue, the rigidity of this device would need to be improved for applications like drilling into harder materials like bone.

Combining the measured targeting error with the tip calibration error and angulation error the resultant targeting error for both the primary and combined registration techniques would be: $142 \pm 41 \mu\text{m}$ and $213 \pm 38 \mu\text{m}$. Including the presence of a 2 N axial load the targeting error would be $149 \pm 41 \mu\text{m}$ and $218 \pm 38 \mu\text{m}$. These estimates of targeting error are better representative of the true targeting error of the robotic system. Even with the inclusion of additional error sources the targeting accuracy of the robot is approximately equal to the imaging voxel size of 153.9 μm . This targeting accuracy makes the robot potentially useful for targeting small vessels with a high degree of confidence. Use of the secondary registration to reduce the time requirements of interventions results in a poorer targeting accuracy which is greater than the image voxel size. This method would be useful for targeting larger structures like the left or right ventricle of a mouse's heart or a large tumor. Since the variability in targeting is relatively low in comparison to the mean error, the targeting accuracy could be further

improved to achieve finer targeting accuracies using micro-CT scanners with smaller voxel sizes. One approach to improve the targeting accuracy is introduced by Ramrath *et al.* [19] to measure the magnitude and direction of needle misalignment using a high-resolution camera. An appropriate correction can then be applied when positioning the needle to reduce error from needle misalignment.

3.4.4 Preclinical Application

Under image-guidance, the robot was able to successfully target a 23G needle to a 1.5mm radio-opaque pellet implanted in a subcutaneous tumour. Tissue deformation was observed during the initial penetration and retraction of the needle, and could potentially result in missing the intended target. While the effect of tissue deformation was negligible when the target was a 1.5 mm radio-opaque pellet, it will likely worsen with smaller targets and when the target is close to the skin (where the observed tissue deformation was the largest). Using real-time image guidance it may be possible to reduce, if not eliminate, the effect of tissue deformation.

The wick-in-needle technique requires proper placement of the needle for reliable IFP measurements in small tumours. Both the front and side ports of the IFP needle must be inside the tumour volume, which becomes difficult in small animal tumours with diameters between 5 to 10 mm. The average distance between the front and side port of our IFP needle was approximately 5 mm. Therefore, a great deal of uncertainty in manually placing the IFP needle in mouse tumours < 10 mm is expected. For example, we have found that performing repeated manual needle placement in an intra-muscular ME180 tumour 7mm in diameter results in IFP values that differ by a factor of 5. In this study, we have shown that the robotic position system in combination with image guidance provides an accurate method to guide needle placement, and reliably perform IFP measurements. Additionally, the design of the robot allows for spatially mapping of IFP over the tumour volume and is an application we plan to explore in the future.

3.5 Conclusion

The design of a micro-CT guided needle positioning system for small animal interventions has been presented. The system has been developed with the objective of

achieving a mean targeting error of $< 200 \mu\text{m}$ while maintaining a high degree of user-friendliness. The robot is compact enough to operate within the micro-CT bore. Small-animals can be imaged and the intervention performed without the need to transport the animal from one workspace to another. Not requiring transport of the animal reduces opportunities for targets to shift from their localized position in the image and simplifies the work-flow of interventions. An improved method of needle calibration is presented which better characterizes the calibration using the position of the needle tip in photographs rather than the needle axis. A calibration fixture was also introduced which dramatically reduces the time requirements of calibration while maintaining calibration accuracy. Two registration modes have been developed to match the robot coordinate system with the coordinate system of the micro-CT scanner. The two registration modes offer a balance between the time required to complete a registration and the overall registration accuracy. The development of slow 'high' accuracy and fast 'low' accuracy registration modes provides the user with a degree of flexibility in selecting a registration mode best suited for their application. The errors of the 'high' accuracy primary registration were $\text{FRE}_{\text{primary}} = 21 \pm 6 \mu\text{m}$ and $\text{TRE}_{\text{primary}} = 31 \pm 12 \mu\text{m}$. The error in the 'low' accuracy combined registration was $\text{TRE}_{\text{combined}} = 139 \pm 63 \mu\text{m}$. Both registration modes are therefore suitable for small-animal needle interventions. The targeting accuracy of the robotic system was then characterized using targeting experiments in tissue-mimicking gelatin phantoms. The results of the targeting experiments were combined with the known calibration and needle deflection errors to provide a more meaningful measure of the needle positioning accuracy of the system. The combined targeting errors of the system were $149 \pm 41 \mu\text{m}$ and $218 \pm 38 \mu\text{m}$ using the primary and combined registrations respectively. Finally, pilot *in vivo* experiments were completed to demonstrate the performance of the system in a biomedical application.

References

- [1] R. H. Taylor and D. Stoianovici, "Medical Robotics in Computer-Integrated Surgery," *IEEE Trans. Robot. Autom.* 19 (5), 765–781 (2003).
- [2] K.B. Stitzenberg, Y. Wong, M. E. Nielsen, B.L. Egleston and R.G. Uzzo, "Trends in Radical Prostatectomy: Centralization, Robotics, and Access to Urologic Cancer Care," *Cancer*, In Press, 2011.
- [3] K. Cleary, A. Melzer, V. Watson, G. Kronreif and D. Stoianovici, "Interventional Robotic Systems: Applications and technology state-of-art," *Minimally Invasiv. Ther.* 14 (2), 101–113 2006.
- [4] T. de la Cueva, A. Naranjo, E. de la Cueva, and D. Rubio, "Refinement of intrathymic injection in mice," *Lab Anim.*, 36(5), 27–32 2007.
- [5] M. El-Ghamari, F. Bergmann, B. M. Schmied, J. Weitz, and A. Ulrich, "Islet Cells Contribute to Pancreatic Carcinogenesis in an Animal Model," *Pancreas*, 40(2), 242-246, 2011.
- [6] M.L. Springer, R.E. Sievers, M.N. Viswanathan, M.S. Yee, E. Foster, W. Grossman and T. Yeghiazarians, "Closed-chest cell injections into mouse myocardium guided by highs-resolution echocardiography," *Am. J. Physiol. Heart Circ. Physiol.* 289 H1307–1314, 1995.
- [7] Q. Li, B. Li, X. Wang, A. Leri, K.P. Jana, Y. Liu, J. Kajstura, R. Baserga and P. Anversa, "Overexpression of Insulin-like Growth Factor-1 in Mice Protects from Myocyte Death after Infarction, Attenuating Ventricular Dilation, Wall Stress, and Cardiac Hypertrophy," *J. Clin. Invest.*, 100(8), 1991-1993, 1997.
- [8] R. Blair-Handon, K. Mueller and S. Hoogstraten-Miller, "An alternative method for intrathymic injections in mice," *Lab Animal*, 39(8), 246-252 (2011).
- [9] V. Horsley and R.H. Clarke, "The structure and function of the cerebellum examined by a new method," *Brain*, 31(1), 45–124 (1908).

- [10] G.C. Kagadis, G. Loudos, K. Katsanos, S. G. Langer and G.C. Nikiforidis, "In vivo small animal imaging: Current status and future prospects," *Med. Phys.*, 37(12), 6421-6437 2010.
- [11] S.J. Schambach, S. Bag, L. Schilling, C. Groden and M.A. Brockmann, "Application of micro-CT in small animal imaging," *Methods*, 50(1), 2-13 (2010).
- [12] S.H. Bartling, W. Stiller, W. Semmler and F. Kiessing, "Small animal computed tomography imaging," *Curr. Med. Imaging Rev.*, 3(1), 45-59 2007.
- [13] C.T. Badea, M. Drangova, D.W. Holdsworth and G.A. Johnson, "In vivo small-animal imaging using micro-CT and digital subtraction angiography," *Phys. Med. Biol.*, 53, R319-350, 2008.
- [14] P. Kazanzides, J. Chang, I. Iordachita, J. Li , C. Clifton Ling and G. Fichtinger, "Development of an image-guided robot for small animal research," *Comput. Aided Surg.*, 12(6), 357–365, 2007.
- [15] S.A. Nicolau, L. Mendoza-Burgos, L. Soler, D. Mutter and J. Maresaux, "In vivo evaluation of a guidance system for computer assisted robotized needle insertion devoted to small animals," *Lect. Notes Comp. Sci.*, 5128, 241-250, 2008.
- [16] A.C. Waspe, D.D. McErlain, V. Pitelka, D.W. Holdsworth, J.C. Lacefield and A. Fenster, "Integration and evaluation of a needle-positioning robot with volumetric micro-computed tomography image guidance for small animal stereotactic interventions," *Med. Phys.* 37(4), 1647-1659, 2010.
- [17] A.C. Waspe, H. J. Cakiroglu, J.C. Lacefield and A. Fenster, "Design, calibration and evaluation of a robotic needle-positioning system for small animal imaging applications," *Phys. Med. Biol.*, 52(7), 1863–1878, 2007.
- [18] M.J. Hwang, O. Bebek, F. Liang, B. Fei and M. Cenk Cavusoglu. "Kinematic Calibration of a Parallel Robot for Small Animal Biopsies," *IEEE Conference on Intelligent Robots and Systems*, 4104-4109, 2009.
- [19] L. Ramrath, U. G. Hofmann and A. Schweikard. "A robotic assistant for stereotactic neurosurgery on small animals," *Int. J. Med. Robot. Comp.* 4(4), 295–303, 2008.

- [20] J. Bax, D. Cool, L. Gardi, K. Knight, D. Smith, J. Montreuil, S. Sherebrin, C. Romagnoli and A. Fenster. "Mechanically assisted 3D ultrasound guided prostate biopsy system," *Med. Phys.* 35(12), 5397-5410, 2008.
- [21] K. Ma, A. Kornecki, J. Bax, Y. Mundt and A. Fenster, "Development and validation of a new guidance device for lateral approach stereotactic breast biopsy," *Med. Phys.* 36(6), 2118-2129, 2009.
- [22] R.H. Taylor, J. Funda, B. Eldridge, K. Gruben, D. LaRose, S. Gomory, M. Talamini, L.A. Kavoussi and J.H. Anderson, "A telerobotic assistance for laparoscopic surgery," *IEEE EMBS Mag.* 14, 279-291, 1995.
- [23] A. Patwardhan, "Subpixel position measurement using 1D, 2D and 3D centroid algorithms with emphasis on applications in confocal microscopy," *J. Microsc.*, 186(3), 246-247, 1997.
- [24] K. S. Arun, T. S. Huang, and S. D. Blostein, "Least-squares fitting of two 3-D point sets," *IEEE Trans. Pattern Anal. Mach. Intell.* PAMI-9(5), 698-700, 1987.
- [25] J. M. Fitzpatrick, J.B. West, C.R. Maurer Jr., "Predicting error in rigid-body point-based registration," *Medical Imaging, IEEE Transactions on* , (17)5, 694-702, 1998.
- [26] L. K. Ryan and F. S. Foster, "Tissue equivalent vessel phantoms for intravascular ultrasound," *Ultrasound in Medicine & Biology*, 23(2), 261-273, (1997).
- [27] H.O. Fadnes, R.K. Reed and K. Aukland, "Interstitial fluid pressure in rats measured with a modified wick technique," *Microvasc. Res.*, 14(1), 27-36, 1977.

Chapter 4

4 Summary and Future Work

4.1 Summary

The purpose of this research project was the development of an image-guided small animal needle positioning robot and its integration with an x-ray micro-computed tomography scanner. The system was developed with the specific goal of surpassing previous efforts for small animal robots in targeting repeatability and user-friendliness while achieving a mean targeting accuracy $< 200 \mu\text{m}$ and being compact enough to operate within a micro-CT bore. The principal technical developments are summarized below.

4.1.1 Chapter 2: Traceable Micro-CT Geometric Accuracy Phantom for Applications Requiring Exact Measurement of Distances or Volumes

The topic of this chapter was the development of a calibration phantom for the routine evaluation of micro-CT geometric accuracy to a traceable standard. The development of the calibration phantom is an important tool for ensuring the success of micro-CT guided small animal robots; such as the system introduced in **Chapter 3**. Geometric errors in micro-CT images will result in incorrect target localization and limit the potential targeting accuracy of these devices. The development of a calibration phantom allows micro-CT users to ensure the highest geometric fidelity in images.

The phantom was constructed from carbon fiber shafts, custom Delrin plastic clamps and 6.35 mm diameter borosilicate beads. A method was developed using gauge blocks which allowed the geometry of the borosilicate beads to be measured to a known and traceable standard of measurement. The phantom was then used to evaluate the geometric accuracy of micro-CT scanners by comparing the bead geometry measured using the gauge blocks to the bead geometry in micro-CT images. The centre of each bead in the micro-CT images was calculated by segmenting the beads using a threshold-based region growing followed by a squared-intensity-weighted centroiding algorithm. A

least-squares solution was then used to calculate scaling factors along each of the scanners three axes to minimize any geometric inaccuracies present in the micro-CT scanners.

The phantom was used to evaluate five micro-CT scanners of four different scanner models. Images of the calibration phantom were processed to calculate the geometric accuracy and appropriate correction factors. To ensure the correction factors were not unique to the calibration phantom, a second validation phantom was constructed. The validation phantom was constructed and measured using the same materials and techniques as the calibration phantom. However, the bead configuration of the validation phantom was different from the calibration phantom. The validation phantom was imaged by each scanner and its beads localized using the correction factors calculated using the calibration phantom. Two of the five scanners were found to have a statistically significant correctable geometric error. For the poorest scanner, the mean geometric error in images of the validation phantom was reduced from a 0.37% to 0.07%. Although this error is small in absolute terms, this correction could be important for applications with demanding geometric accuracy requirements. Regardless of whether a scanner possessed a correctable error, use of the calibration phantom allowed for traceable calibration of the scanner along all three axes.

The principal contribution of this chapter was the development of a phantom design and algorithm which is capable of calibrating the geometric accuracy of all three axes of a micro-CT scanner to a known and traceable standard of measurement. Chapter 2 is the basis of a paper in preparation for submission to the peer reviewed journal *Medical Physics*.

4.1.2 Chapter 3: 3D Image-Guided Robotic Needle Positioning System for Small Animal Interventions

This chapter describes the design of a robotic needle positioning systems, its integration with a commercial micro-CT scanner and the characterization of the system's performance. The robot contains a total of 6 degrees of freedom that consist of 3 linear translational axes, 2 rotational axes and a linear needle driver. The two rotational axes

are created using a kinematic frame based on a spherical linkage design. The rotational axes intersect at a common point in space known as a remote centre of motion (RCM). The entire system mounts onto the bed of the micro-CT scanner and is fully capable of completing interventions within the scanner bore.

A method was developed to calibrate a needle tip to the RCM of the robot. The calibration was accomplished using a calibration fixture. The calibration was validated with photography using a camera equipped with a macro lens. The calibration error was measured to be $\Delta_x=36 \mu\text{m}$, $\Delta_y=70 \mu\text{m}$ in the roll plane and $\Delta_y=11 \mu\text{m}$ and $\Delta_z=5 \mu\text{m}$ in the pitch plane. The repeatability of the needle driver in positioning the needle tip was $\sigma_{\text{needle}}=\pm 9.1 \mu\text{m}$.

A registration process with two different registration methods was developed to register the robot to the micro-CT scanner. The primary registration is the most accurate registration but also takes the most time to perform. The primary registration is also no longer accurate if the robot is removed from the micro-CT scanner bed. To allow a primary registration to be reused after the robot is removed from the micro-CT bed, it can be combined with a secondary registration. The secondary registration can be calculated quickly with only a single image but at the expense of registration quality. The primary registration errors were $\text{FRE}_{\text{primary}}= 21 \pm 6 \mu\text{m}$ and $\text{TRE}_{\text{primary}}= 31 \pm 12 \mu\text{m}$. The secondary registration errors were $\text{FRE}_{\text{secondary}}= 70 \pm 25 \mu\text{m}$ and $\text{TRE}_{\text{secondary}}= 79 \pm 14 \mu\text{m}$. The error of a combined primary and secondary registration was $\text{TRE}_{\text{combined}}=139 \pm 63 \mu\text{m}$.

The targeting accuracy of the robot was next characterized using tissue-mimicking gelatin phantoms. The first set of targeting experiments consisted of targeting points in the phantom at a fixed needle angle. The accuracy was calculated by measuring the distance of the needle axis to the desired target in micro-CT images. The targeting accuracy using a primary registration was $131 \pm 25 \mu\text{m}$. The targeting accuracy using a combined registration was $206 \pm 20 \mu\text{m}$. The second targeting experiment consisted of fixing the translational axes of the robot, inserting a needle into the phantom at angles over the robot's angular range of motion and imaging the needles using micro-CT. The

distance of the needle axes to a point of best fit was calculated. The mean distance of the needle axes to the point of best fit was 71 μm with a smallest distance of 24 μm and largest distance of 189 μm . These targeting accuracies were combined with one another and the other measured sources of error to approximate the overall targeting accuracy of the system to be $149 \pm 41 \text{ }\mu\text{m}$ using a primary registration and $218 \pm 38 \text{ }\mu\text{m}$ using a combined registration.

The chapter finally demonstrates the capability of the robot to complete selected biomedical applications. The robot was able to successfully position a probe under image guidance to perform interstitial tissue pressure measurements in a mouse tumour. The robot was also able to successfully position a needle under image guidance to contact a 1.5 mm bead implanted in dorsal subcutaneous tissue of a mouse.

The principal contribution of chapter 3 was the development of a small-animal robot compact enough to operate within a micro-CT bore and the associated methods to calibrate the robot and register it with the micro-CT scanner. Chapter 3 is the basis of a paper in preparation for submission to the peer reviewed journal *Medical Physics*.

4.2 Conclusion

The field of small animal image-guided robotic systems is in its infancy. The previously developed systems in the field consist largely of initial prototypes which have seen limited adoption by their target audience of preclinical researchers. The preceding chapters have attempted to introduce a number of refinements to small animal robots to better facilitate their adoption among preclinical researchers. The focus of these refinements was achievement of a desirable targeting accuracy with minimal variability within a user friendly system.

A phantom was developed that allows for the routine evaluation of micro-CT scanners. The phantom allows for the user of the robot to quickly evaluate the geometric accuracy of a micro-CT scanner to a traceable standard and apply corrections as necessary. No other small animal image-guided robotic system has validated the geometric accuracy of its selected imaging modality. Use of the phantom provides an

important foundation towards the successful completion of image-guided interventions. Although the phantom was initially developed for use with image-guided interventions, it should prove equally useful for a wide range of micro-CT applications such as the characterization of medical devices.

The robotic system introduced in this thesis offers a number of benefits over previous designs. The robot is compact enough to operate entirely within the micro-CT bore. Specimens are not required to be moved between the imaging and robot workspace as in previous designs. This reduces the time required to complete interventions and reduces errors associated with detaching and reattaching beds. A calibration fixture was developed that allows the robot to be calibrated in a fraction of the time required to calibrate other designs. A dual mode registration method was introduced to offer the user greater flexibility between the time requirements of completing registration and the registration accuracy depending on the requirements of the application. Finally, the robot was demonstrated as achieving the desired $< 200 \mu\text{m}$ targeting accuracy with reduced variability than previous designs.

4.3 Future Work

A number of refinements to small animal image-guided robotic systems were introduced in this thesis. However, a number of potential avenues exist that could further improve the utility of these devices. Several of these avenues are discussed below.

4.3.1 Improved Software Integration and Intervention Planning

Much of the focus of this thesis has been on the development of new processes and procedures for image-guided small animal robotics. As a result, the software developed has the potential for a number of improvements. Currently, several discrete software programs exist to complete an intervention. The user first calculates the robot to micro-CT registration using one program. The results of the registration must then be loaded into a program that displays micro-CT images and allows target localization in robot coordinates. The user must then manually enter the target coordinates into a third program to position the needle at the target. The discrete nature of the software increases

the time required to complete an intervention and opportunities for user error to occur. Integration of the software into a single graphical user interface (GUI) would eliminate these issues.

The intervention planning software could benefit from a number of improvements. Currently, the user visualizes the micro-CT image slice-by-slice in 2D. The user then selects the desired voxel in the image to target and uses a registration to determine the appropriate robot coordinate for the target voxel. Within the software, the user cannot visualize the image in 3D to select a target. The software also does not provide visualization of needle trajectory or the ability to calculate appropriate angulations of the robot for a desired trajectory. Rather, needle trajectory is manually controlled by the user who adjusts the trajectory by eye. Improvements to image and needle trajectory visualization would give the system capabilities similar to clinical systems previously developed within the Fenster laboratory [1].

4.3.2 Integration of Robot with Alternative Imaging Modalities

In addition to micro-CT, the robotic system could be integrated with additional small animal imaging systems. Two modalities of particular interest are magnetic resonance (MR) and ultrasound. Each of these modalities offers distinct benefits when compared to micro-CT imaging [2]. Integration of the robot with ultrasound would require limited modification of the robot mechanical design. However, the registration technique developed for micro-CT could not be applied for ultrasound guidance. Development of a method to register the robot presents the primary challenge to integration with ultrasound. Work within the lab has been initiated to develop a registration technique based upon the techniques developed by Waspe *et al.* for small animal interventions [3]. Integration of the robot with MR imaging presents the opposite challenge to ultrasound. The micro-CT registration technique should be translatable to MR with the selection of an appropriate fiducial with high MR contrast. However, the mechanical design and materials of the robot would require modification to attain MR compatibility. A preliminary design has been developed within the lab for an MR compatible robot consisting of non-magnetic materials and powered by ceramic motors.

4.4 Final Remarks

As the capabilities and usability of image-guided robots for small-animal applications grow, the field of preclinical research can be expected to reap a number of benefits. Robots extend the abilities of preclinical researchers by offering the ability to position needles with greater repeatability and accuracy while reducing invasiveness over conventional techniques. Furthermore, robots offer an improvement to the overall efficiency of preclinical research by allowing interventions to be completed with less cost and time. The device and techniques developed in this research project offer a number of refinements to improve the performance and user-friendliness of image-guided small animal robots. None the less, small animal image-guided robotics remains a field in its infancy and much future work exists before the full potential of these benefits is experienced.

References

- [1] J. Bax, D. Cool, L. Gardi, K. Knight, D. Smith, J. Montreuil, S. Sherebrin, C. Romagnoli and A. Fenster. "Mechanically assisted 3D ultrasound guided prostate biopsy system," *Med. Phys.* 35(12), 5397-5410, 2008.
- [2] G.C. Kagadis, G. Loudos, K. Katsanos K, S.G. Langer and G.C. Nikiforidis, "In vivo small animal imaging: Current status and future prospects," *Med. Phys.*, 37(12), 6421-6437, 2010.
- [3] A.C. Waspe, J.C. Lacefield, D.W. Holdsworth and A. Fenster, "Registration of a needle-positioning robot to high-resolution 3-D ultrasound and computed tomography for image-guided interventions in small animals," *Proc. SPIE 6918*, article 691807, 2008.

Curriculum Vitae

Name: Christopher Stanley Robert Waring

EDUCATION

2009-2012 **University of Western Ontario**, London On Canada
Master of Engineering Science (M.E.Sc).
Biomedical Engineering Graduation Program

2004-2009 **University of Western Ontario**, London On Canada
Bachelor of Arts (B.A.)
Major in History with Distinction
Faculty of Social Science

2004-2009 **University of Western Ontario**, London On Canada
Bachelor of Engineering Science (B.E.Sc.)
Mechanical Engineering with Distinction
Department of Mechanical and Materials Engineering

TEACHING EXPERIENCE

Fall 2010 **University of Western Ontario**
MME 2259a: Product Design and Development
Teaching Assistant, 70 Hours

Fall 2009 **University of Western Ontario**
MME 2259a: Product Design and Development
Teaching Assistant, 70 Hours

INDUSTRIAL EXPERIENCE

Summer 2008 **General Dynamics Land Systems Canada**, London On Canada
Customer Support Services
Summer Student

Summer 2007 **General Dynamics Land Systems Canada**, London On Canada
Quality Assurance
Summer Engineering Co-op Student

Summer 2006 **General Dynamics Land Systems Canada**, London On Canada
Quality Assurance
Summer Engineering Co-op Student

Summer 2005 **General Dynamics Land Systems Canada**, London On Canada
 Quality Assurance
 Summer Engineering Co-op Student

SCHOLARSHIPS

2009-2011 NSERC-CREATE Training Program in Computer Aided Medical
 Intervention (\$9000/year for 2 years)
 University of Western Ontario

2009-2011 Western Graduate Research Scholarship (Tuition Deferral)
 University of Western Ontario

2004-2005 Western Scholarship of Excellence (CAN \$2000)
 University of Western Ontario

2003-2004 Western's Initiative for Scholarly Excellence (Tuition Deferral for
 One Full Year Course)
 University of Western Ontario

PUBLICATIONS AND PRESENTATIONS

A. Proffered Conference Presentations

1. Christopher Waring, Jeffrey S. Bax, Amila, Samarabandu, David W. Holdsworth, James C. Lacefield and Aaron Fenster, "Micro-CT Geometric Accuracy Phantom for Improved Fiducial Localization in Image-Guided Needle Positioning Systems", 2011 Joint AAPM/COMP Meeting, Vancouver BC: July 31-August 4, 2011, Med. Phys., 38(6), p 3376.
2. Christopher Waring, Jeffrey S. Bax, Amila, Samarabandu, David W. Holdsworth, James C. Lacefield and Aaron Fenster, "Micro-CT Geometric Accuracy Phantom for Improved Fiducial Localization in Image-Guided Needle Positioning Systems", 6th Canadian Student Conference on Biomedical Computing and Engineering, London ON: May 26-28, 2011, 6th Annual CSCBCE Conference Proceedings, p 46-50.
3. Christopher Waring, Jeffrey S. Bax, Jacques Montreuil , James C. Lacefield and Aaron Fenster, "Micro-CT Geometric Accuracy Phantom for Improved Fiducial Localization in Image-Guided Needle Positioning Systems", Imaging Network of Ontario 9th Annual Symposium, Toronto ON: January 31- February 1, 2011.

B. Proffered Poster Presentations

1. Christopher Waring, Jeffrey S. Bax, Jacques Montreuil , James C. Lacefield and Aaron Fenster, "3D Image-Guided Robotic Needle Positioning System for Small Animal Interventions", London Imaging Discovery Day (LID), London, ON: June 23, 2011.

2. Christopher Waring, Jeffrey S. Bax, Jacques Montreuil , James C. Lacefield and Aaron Fenster, “3D Image-Guided Robotic Needle Positioning System for Small Animal Interventions”, London Imaging Discovery Day (LID), London, ON: June 17, 2010.
3. Christopher Waring, Jeffrey S. Bax, Jacques Montreuil , James C. Lacefield and Aaron Fenster, “3D Image-Guided Robotic Needle Positioning System for Small Animal Interventions”, Margaret Moffat Research Day, University of Western Ontario, London, ON: March 31, 2010.
4. Christopher Waring, Jeffrey S. Bax, Jacques Montreuil , James C. Lacefield and Aaron Fenster, “3D Image-Guided Robotic Needle Positioning System for Small Animal Interventions”, Imaging Network of Ontario 8th Annual Imaging Symposium, Toronto, ON: February 1-3, 2010.